University of Arkansas, Fayetteville

ScholarWorks@UARK

12-2015

Image Processing and Visualization of Terahertz Pulsed Imaging of Breast Cancer Tumors

Yuhao Wu
University of Arkansas, Fayetteville

Follow this and additional works at: https://scholarworks.uark.edu/etd

Part of the Biomedical Commons, and the Biomedical Devices and Instrumentation Commons

Citation

Image Processing and Visualization of Terahertz Pulsed Imaging of Breast Cancer Tumors

A thesis submitted in partial fulfillment
of the requirements for the degree of
Master of Science in Computer Science

By

Yuhao Wu
University of Arkansas
Bachelor of Science in Computer Science, 2014
University of Arkansas
Bachelor of Science in Mathematics, 2015

December 2015
University of Arkansas

This thesis is approved for recommendation to the Graduate Council.

_____
Dr. John Gauch
Thesis Director

_____   _____
Dr. Gordon Beavers   Dr. Magda O. El-Shenawee
Committee Member   Committee Member

_____
Dr. Christophe Bobda
Committee Member

Abstract

Terahertz imaging technology has grown substantially in recent years. With new advances made in the generation, manipulation, and detection of terahertz radiation, terahertz imaging has found its application as inspection tools in a wide range of areas including biomedicine, materials science, and aerospace industries. In the field of medical imaging, terahertz (THz) has emerged as a new imaging modality due to some fundamental physical properties of the THz wave. THz imaging has been used to examine various biological structures, and THz tomography has been developed to probe the 3D structures of those samples.

THz pulsed imaging (TPI) is one of the THz imaging technologies that have been developed and used to inspect different types of biological structures. Specifically, it has been used to examine breast cancer tumors in hope of providing accurate, fast, and convenient diagnosis. Several works have been published in this research area that demonstrate the potency of THz imaging in differentiating tumor regions from healthy tissue regions. Most of the current research, however, focuses on the improvement of the instrumentation of THz imaging system or the study of the electrical and optical properties of the tissue samples being imaged. In this work, we seek to analyze the scanned image data and improve the visualization of them through image processing and segmentation techniques. We apply a variety of image enhancement and segmentation algorithms to our gathered data and evaluate how effective they are at visualizing the scanned samples and classifying the tissue regions. Our experimental results show that several image processing techniques can be utilized to help us visualizing the detailed structures of the scanned tissues and extract useful information which can be used for identifying tumor boundaries. The result of this work further demonstrates the possibility of adapting THz imaging system in real-world clinical settings that may facilitate the diagnosis of breast cancer.

Acknowledgements

I would like to thank Dr. Gauch and Dr. El-Shenawee for the opportunity to conduct this research with them as well as their guidance throughout my graduate education. I also would like to thank Dr. Beavers and Dr. Bobda for reviewing my thesis and being on my thesis committee.

I would like to thank the THz Imaging and Spectroscopy Research Group of the Electrical Engineering Department at the University of Arkansas for providing me with all the THz image data and experimental measurements. I would like to thank Tyler Bowman in particular for collecting all the THz data and continuously helping me throughout the research.

I would like to thank the rest of the faculties and staffs in the CSCE department at the University of Arkansas for their generous help and continuous support throughout my undergraduate and graduate years.

I would like to thank all my friends I get to know here at the University of Arkansas for their sincere suggestions and all the fun we had together.

Finally and most importantly, I would like to thank my parents for raising me to be who I am, and for always being source of endless inspirations.

Table of Contents

I.   Introduction

A.   Problem and Motivation

Breast cancer is the second most prevalent cancer among American women, preceded only by skin cancer [1]. According to the statistics from American Cancer Society, about 1 out of 8 women in the US will develop invasive breast cancer during their lifetime. It is estimated that about 300,000 new cases of invasive and non-invasive breast cancer will be diagnosed in the US in 2015, and about 40,000 women will die from breast cancer. Two types of surgical operations are usually involved in the treatment of breast cancer. Breast-conserving surgery (BCS), sometimes referred to as partial (or segmental) mastectomy, removes cancer as well as some surrounding normal tissue from the part of breast that contains tumor. Mastectomy, on the other hand, removes entire breast in cases where BCS is not sufficient to preventing the spreading of cancer. In BCS, the tissue part that is removed is reexamined by a pathologist, and if cancer cells are found at any of the edges of the removed tissue, it is said to have positive margins. Positive margins usually indicate that some cancer cells may have been left in the breast after surgery. A second surgery called re-excision is needed to remove more tissue to ensure that no cancer cells are left behind. Studies have shown that using current imaging techniques such as preoperative mammography and magnetic resonance imaging (MRI), positive margins occur in 20% to 40% of the patients that underwent BCS, and the additional surgeries incur negative impact on the cosmetics, psychological distress, and health costs of the patients [2]. This significant occurrence rate of positive margins is largely due to lack of real-time intraoperative information of the presence of positive margins during BCS. Although currently there are some intraoperative analysis methods employed to assess tissue margin conditions, the complications and instabilities involved with these analysis methods certainly raise the need for more accurate and easy-to-use

1

surgical methods to be developed. Some emerging technologies such as positron emission tomography imaging and near-infrared fluorescence optical imaging have been developed. With the maturation and expansion of THz imaging technology, several studies have been conducted that applied THz imaging to breast cancer tumors [3][4][5][6][32]. The results from these studies have shown the theoretical viability of using THz imaging to inspect excised breast tissues and identify tumor margins. For an actual THz imaging system to be deployed under a surgical setting, however, there are other obstacles that need to be cleared before a real-time THz system can be effectively used during a surgical operation. Specifically, there needs to be a data processing pipeline that takes the data gathered from the THz scanner and produces proper visualizations of the image data in order to help pathologists and surgeons locate the tumors and identify whether positive margins exist in the excised tissues. The objective of this thesis is to explore the effectiveness of some of the image processing and visualization techniques on image data gathered from THz scans of breast cancer tumors.

B.   Thesis Statement

In this work, we applied a number of image enhancement and visualization techniques for pulsed terahertz images of breast tissues that have been diagnosed as triple negative infiltrating ductal carcinoma (IDC). We obtained the THz scanned images of tissue slices and blocks from Dr. Magda O. El-Shenawee's Terahertz Imaging and Spectroscopy research group in the Electrical Engineering Department at University of Arkansas. The image data were processed by our own C++ programs as well as some existing visualization packages. We evaluated how various processing techniques can assist us at extracting useful information about the structure of the scanned samples, and how effective they are at producing clear and sensible 2D and 3D visualizations of the imaged tumors. For any particular processing technique we investigated, we

2

also experimented how different input parameters can affect the output of the processing. Our experiment results demonstrate that several image processing techniques can be used to generate visualizations of pulsed THz scans of breast cancer tumors that contain distinguishable details, and image segmentation algorithms can be further employed to differentiate tumor regions from healthy tissue regions.

C.   Thesis Organization

Chapter 2 gives a background about THz technology and its application in medical imaging. Several traditional diagnostic methods used in BCS are also surveyed and how recent related works have shown THz imaging as a promising candidate for the detection of positive margins in BCS. Chapter 3 explains the approaches taken to analyze the gathered data as well as the implementations of the processing and visualization in our own C++ programs and other existing visualization software. Chapter 4 evaluates the results of our processing and visualization methods. Finally, Chapter 5 presents our conclusions and discusses our future work in this area.

II.   Background and Related Work

A.   Terahertz Imaging Technology

What is Terahertz Radiation?

Terahertz (THz) radiation, also known as terahertz wave or T-ray, refers to the part of the electromagnetic spectrum around the frequency range of 1 THz (1 THz = 10^{12} Hz). This frequency range, which is sometimes called the "THz gap", is commonly defined to be from 0.3 THz to 3 THz, although slight variations on this definition exist in the literature [7]. THz waves are sometimes called submillimeter waves since 0.3 THz corresponds to 1 mm in the wavelength, and wavelength decreases as frequency increases beyond 0.3 THz. This terahertz gap falls in between the band regions of infrared and microwave in the electromagnetic spectrum. The term "gap" also refers to the fact that only until recently there was no consistent method to generate and detect THz waves [8]. Even though successful technologies had already been developed for the infrared and microwave radiations, THz band remained as an unexplored territory until breakthroughs were made a few decades ago. There are abundant sources of THz radiation in the nature. For instance, the black-body radiation from any warm object includes frequency in the THz band [8]. More importantly, recent development in THz technology has made a number of artificial devices as viable sources of THz radiation as well.

THz Imaging as a New Modality

The idea of using THz radiation for imaging purposes was not surprising given the fact that both infrared and microwave radiations had been successfully exploited to image various objects. This idea, however, was faced with great challenges back in the 1960s and early 1970s when there was a lack of methodologies for generating, manipulating, and detecting THz waves [9]. Advancement made in laser technology in the 1970s and 1980s facilitated the development

of new terahertz system that was able to produce much brighter and tunable THz radiations. The work ultimately led to the invention of terahertz time-domain spectroscopy (THz-TDS), in which a short pulse of THz wave is emitted to probe the structure of the imaged sample. This is also the method by which our scanned data were obtained. The first images acquired from THz-TDS were reported by Hu and Huss in 1995 [10]. Since then, THz imaging technology has expanded quickly. Improvements have been made in the generation and detection of THz waves. THz imaging has found its applications in a vast number of fields, including pharmaceutics, security, materials characterization, and aerospace industries. New imaging techniques have been developed, such as continuous-wave THz imaging and THz tomography.

The growth and maturation of THz imaging has made it become a new modality in medical imaging. There are several key characteristics THz imaging has that make it especially appealing in medical imaging. One of the most important advantages of THz imaging is its diagnostic capabilities [11]. Different types of soft tissues react differently to THz pulses, which can be potentially used to categorize various tissue structures. Another major advantage of THz imaging is its versatility in terms of that we can form a variety of images based on the data we measured, e.g. panchromatic-absorption images, refractive-index images, and time-of-flight images. Given the wavelengths of THz waves which are shorter than microwaves and longer than infrared, THz waves offer better spatial resolution compared to microwaves and exhibit less Rayleigh scattering compared to infrared, thus in principle better image qualities can be achieved by using THz imaging. THz radiation also resides on the non-ionizing portion of the EM spectrum, thus it does not have the safety risks that are involved with X-ray and Gamma ray imaging. Additionally, the cost involved in THz imaging is relatively low compared to the

expensive methodologies such as MRI, and we expect its cost to decrease further as THz technology grows and cheaper equipment is made.

THz imaging has found a plethora of applications in a wide range of areas, such as biological imaging, nondestructive testing (NDT), security scanning, and package inspection [12]. For instance, THz waves can reveal useful information about the composition of polymers and thus can be used in the production process of plastics. THz has found a lot of applications in NDT, especially in the aerospace industry [13]. It has been successively used to detect defects in spacecraft. Another study has shown that THz can be used to detect and segment concealed objects such as kitchen knife and metallic handgun [14], demonstrating its potential in future security screening applications. In particular, the number of THz imaging applications in the field of medical imaging is growing. Woodward et al. has used THz pulsed imaging (TPI) to study human skin tissue and skin cancer. They exploited the high sensitivity of THz radiation to polar molecules such as water to examine the hydration levels in the skin, which can be used to determine the lateral spread of skin cancer pre-operatively [15]. Several studies have reported that good contrast between healthy and cancerous tissues is obtained when applying THz imaging to excised colon tumors [16][17]. Other applications include THz imaging of teeth, brain tissue, and other animal tissues [18][19][20]. In this study, THz images of breast cancer tumors are considered.

There are currently two major paradigms in THz imaging depending on the type of laser source used – continuous wave (CW) imaging and pulsed time-domain imaging. In CW imaging, a single fixed or several discrete frequency outputs that are tunable are produced to generate a continuous THz wave [7], whereas in pulsed imaging, broadband emission of THz waves that range across several THz of frequency is produced as ultrashort, sub-100 femtosecond pulses

[12]. CW systems can usually generate images of higher spectral resolution. Since only the intensity of the transmitted energy is measured, its scanning speed is fast and processing of the recorded data is relatively straightforward. In some applications when only the intensity information is needed and resolution is a priority, CW is a better choice in terms of the simplicity, speed, and cost it offers [21]. Pulsed imaging, on the other hand, provides a much richer measurement since a whole waveform of electrical field is recorded in the time-domain for every single point of measurement. Depth, time-domain, and frequency-domain information can be extracted from the gathered data, which allows us to better understand the imaged samples. The tradeoffs for pulsed method are image resolution, measuring speed, and equipment cost. Besides these two imaging methodologies, there is also a distinction in the detection geometry. Depending on whether the THz detector is located on the same side of the sample as the emitter, we have reflection mode when they are both on the same side and transmission mode when they are on the opposite side. In this paper, all of our sample data are scanned using a THz pulsed imaging system, and most of them are measured under the reflection mode.

B. **Breast Conserving Surgery**

Breast conserving surgery (BCS), also called lumpectomy, is the common method to treat breast cancer when only the part of breast that contains the tumor needs to be removed [1]. In BCS, the tumor is excised along with a rim of normal breast tissue to ensure that no cancer is left behind in the breast. When cancer cells are found at any of the edges of the removed tissue, the tissue is said to have a positive margin. A positive margin usually requires a second surgery to remove enough of more tissue to get a clear margin, which puts extra medical costs and mental burdens on the patients. Ideally, we want to eliminate the need for a re-excision as much as possible. In order to achieve this, we need to have reliable methods to assess the margin

conditions. Currently, there are several imaging techniques that are employed to help surgeons decide whether positive margins exist. The standard procedure is to prepare slices of excised tumor tissue to be examined by a pathologist after the surgery [3][4]. Since the slices need to be frozen prior to examination, the pathology report usually requires a few days to get ready. Preoperative mammography is another common way of assessing tumor location and size. It is often used with ultrasound to get some information about the growth of cancer before surgery. Some studies have shown, however, that they both fail to accurately assess the extent of cancer, especially in younger women [2]. MRI, on the other hand, can provide better accuracy in assessing the size of tumor and higher differential power in distinguishing malignant tissue from fibrosis, especially in younger women [2]. Possibly due to the lack of real-time assessment during the surgery, the outcome of BCS failed to show a significant improvement even with the assistance of MRI prior to the operation [2]. A number of intraoperative procedures have been developed to gain information about tissue margins as well. Wire-guided localization, which has been the standard technique for intraoperative tumor localization for more than 20 years, is considered ineffective in BCS for several reasons such as inaccuracy and error prone [2]. Other techniques, such as ultrasound-guided resection and specimen radiography, also demonstrate certain limitations that prevent them from wide adaptation in BCS [2]. Frozen section analysis (FSA) is another popular intraoperative pathological margin assessment in many oncologic procedures. While FSA can reduce the rate of re-excision in some cases and is relatively cheap to perform, it requires a relatively large portion of the specimen and usually increases the duration of the surgery [2]. Less common techniques include touch preparation cytology and standardized cavity shaving, the effectiveness of both approaches are still questionable [2].

Several innovative imaging technologies are explored to address the need for a better intraoperative margin assessment. While positron emission tomography (PET) has the advantage of high sensitivity and specificity for certain types of breast tumors, its use is limited by factors such as spatial resolution, cost, and radiation exposure [2]. Other techniques such as radio-guided occult lesion localization and near-infrared fluorescence optical imaging have also demonstrated great potentials in intraoperative margin assessment, even though more extensive studies are still being conducted to overcome the limitations associated with them and before wide spread applications are possible [2].

In this work, we will focus on the application of THz imaging in breast cancer diagnosis. Specifically, we would like to investigate how well THz imaging can be potentially used to assist surgeons in the margin assessment during BCS. Several previous studies have shown its capability to distinguish between cancerous and healthy tissues. Fitzgerald et al. [6] conducted research on 22 excised human breast tissue specimens with carcinoma and found that strong correlations exist between the size and shape of tumor regions on THz images and those on photomicrographs obtained from histopathologic examination. Ashworth et al. [5] measured the complex refractive indices of freshly excised breast tissue collected from 20 patients in the 0.15 – 2.0 THz range among healthy tissue and cancerous tissue. Their experiment showed that samples containing cancer have higher refractive index and absorption coefficient in the THz range. THz imaging can thus be used to differentiate between healthy and cancerous regions due to their fundamentally different optical properties. Bowman et al. [3][4] used THz pulsed imaging in reflection mode to examine breast tissues of various thicknesses that were diagnosed as triple negative infiltrating ductal carcinoma (IDC). The samples were fixed in formalin, embedded in paraffin, and scanned by TPI systems with several step sizes. The measured THz

9

field responses at each pixel were validated with the Fresnel reflection coefficient formulation and comparison was made against standard histopathology images. St. Peter et al. [32] experimented with single frequency THz radiation and evaluated its ability to discern malignant from benign tissues in reflection mode. The THz images obtained were correlated with standard histological micrographs and a mean discrimination of 73% was found for five out of six samples scanned using Receiver Operating Characterization (ROC) analysis. All these previous results suggest that THz imaging has the capability to differentiate between healthy and cancerous regions in breast tissue, and with future development of THz technology, THz imaging system may be used by surgeons to provide a real-time assessment of margin conditions in excised breast tumors. In the next section, we describe how image processing and visualization can be applied to THz images to aid in the detection of positive margins in breast cancer tissue.

III.   Approach and Implementation

A.   Data Acquisition

All image data were collected and provided by Dr. Magda O. El-Shenawee's THz Imaging and Spectroscopy research group in the Department of Electrical Engineering at University of Arkansas using a TPS Spectra 3000 imaging system [3][4]. Histopathology images for some of the imaged samples were also acquired for validation purpose. To generate a THz image of a tissue sample, the sample being imaged was mounted flat on a movable stage and raster scanned to measure the reflected or transmitted waveform at each pixel location in a defined x-y plane. The measurement of each of these time-domain pulses was first deconvolved using either the gold mirror reference or the glass slide reference to minimize the effects of system noise and background reflection. A low-pass (LP) filter was also utilized to avoid low-signal errors at higher frequencies of the reference [3][4]. 3D THz images were then generated from the preprocessed signals. The x-y plane of a THz image corresponds to the spatial domain in which the imaged sample was raster scanned. At each pixel location in the x-y plane, a whole waveform of data was recorded that contains all the measurements from a single pulse in its time domain.

The scanned image data are stored in so-called TVL files which can only easily be processed by the software package that comes along with the TPS imaging device. In order for us to apply our image processing visualization techniques later on, we have to extract the data contained in these TVL files first and store them in some other convenient format that can be readily processed by our C++ programs as well as other third-party visualization packages. We chose a RAW file format, in which only the actual measurement values are stored in a 3D array data structure. This simple storage scheme works well, as it is easy to locate a neighborhood of

11

pixels/voxels, which is required by most of the spatial filtering techniques we implemented. $f(y, x, t) = data[y][x][t]$ is the measurement value of the voxel located at y rows down, x columns to the right in the spatial domain, and the tth measurement taken in the time domain. All of our samples originally contain 1024 measurements in the time domain at each of the spatial locations within the images.

B.   Cross-Section Data Visualization

There are several techniques that we can use to visualize our image data as 2D images. A straightforward way is to look at 2D cross-sections of the 3D voxel values. We can choose which dimension to keep fixed while mapping all the values in the other two dimensions onto a plane. To see pulsed waveform in time domain, we fix either x or y to some arbitrary position and map all the voxels with that fixed coordinate onto pixels of a 2D image. For example, if we select $x = x_0$, we can generate the 2D image $f(y, t)$ such that $f(y, t) = f(y, x_0, t)$.Similarly, if we select $y = y_0$, we can generate the 2D image $f(x, t)$ such that $f(x, t) = f(y_0, x, t)$. This visualization approach is illustrated by the image on the right of Figure 3.1. If we want to visualize a cross section image in time-domain at time $t = t_0$, we can generate the 2D image $f(y, x)$ such that $f(y, x) = f(y, x, t_0)$. By interactively changing the cross-section coordinate x_0, y_0, t_0 the user can visualize different portions of the 3D data to better understand the structures within the imaged sample.

One subtle thing is that the data values in the TVL images represent electrical field properties of the detected THz signals, and they generally have floating point values between (-15.0, 15.0). Since most image display software expect intensity values in the integer range of [0, 255] or the floating point range of [0, 1] for greyscale images, we must scale our raw data values into the appropriate range prior to display. To do this, we use the linear scaling equation

$f'(y, x) = \frac{f(y,x) - min}{max - min} * 255$ to map all the electrical field values in the input image within

intensity range [min, max] into [0, 255] or simply $f'(y, x) = \frac{f(y,x) - min}{max - min}$ to map into [0, 1]. We

can use our own C++ program to scale manually, or we can use other visualization packages to

handle the scale automatically.

MeVisLab is one of the main tools we experimented with to help us processing as well as

visualizing our image data [23]. It is a modular image processing framework focused on medical

imaging research. It already has built-in libraries of image processing modules that can be

utilized for a variety of processing tasks, and we will demonstrate several applications of some of

the features and functionalities in the following sections.
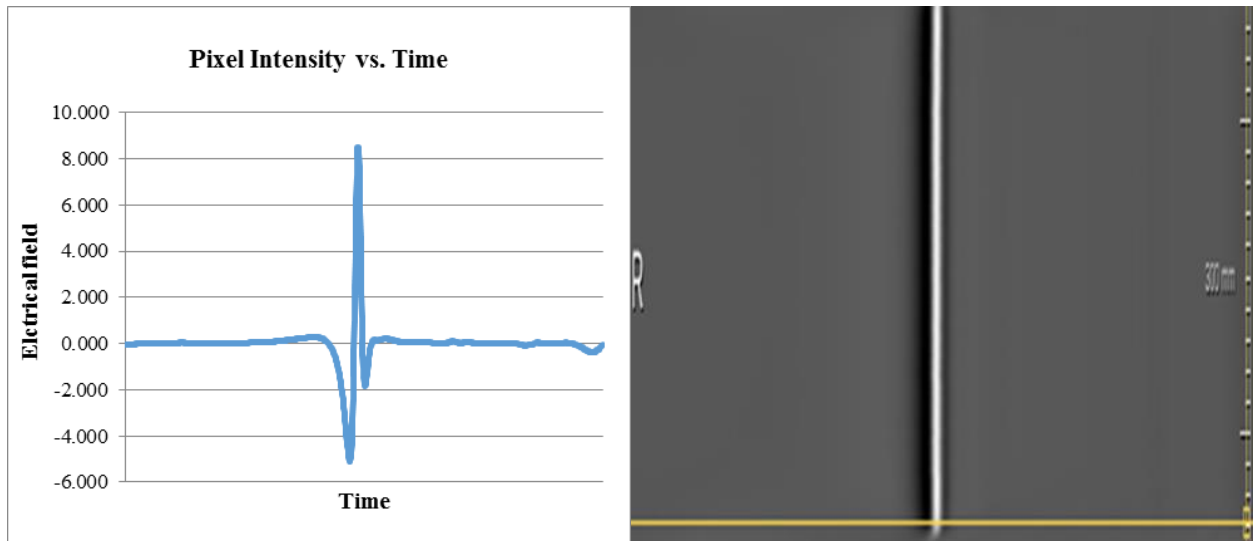
Figure 3.1: The pulsed waveform measured in time domain. The image on the left shows a typical plot of recorded electrical field values as a function of time at some arbitrary spatial location in our THz images. The 2D image on the right shows a typical side view (i.e. when either *y*-coordinate or *x*-coordinate is fixed) of our THz data. In this image, horizontal direction corresponds to time domain and vertical direction corresponds to either *x*- or *y*-coordinate.

C.   Image Enhancement

Scanline Registration

While reading the raw data from the TVL files, some inherent data inconsistencies were noticed. First, the number of time-pulse samples in each image row (*x*-direction) is not consistent across the image. There are roughly the number of time-pulse samples as specified in the header of the corresponding TVL file for each *y*-coordinate, but frequently there are either a few more or less samples than the header specified. Time-pulse samples on the left or right edge of the image are either truncated or repeated in cases of extra or missing sample readings. Second, there are some misalignments between the odd and even scanlines of the data. This introduces a zig-zag artifact in the image (Figure 3.2). To correct this problem, we calculate the mean squared error (MSE) for each odd row with its adjacent even rows and shift each odd row adaptively by [-3, 3] pixels based on the shift amount that gives the minimal local MSE.
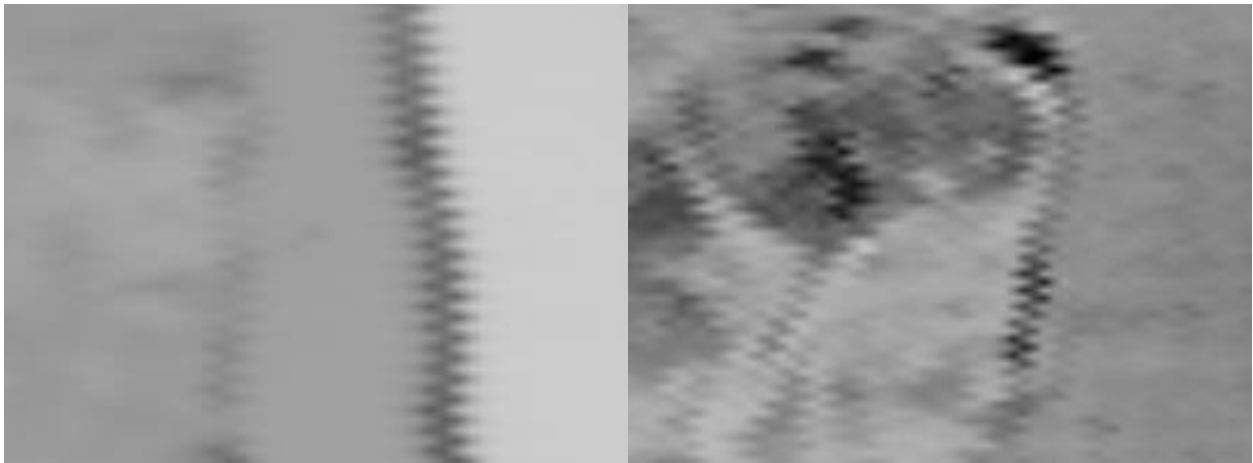

Figure 3.2: Inconsistency in the image rows causes a zig-zag artifact in our THz image data.

Intensity Windowing

Intensity windowing is a contrast enhancement operation that maps only a subrange of pixel/voxel values into the displayed intensity levels instead of mapping the whole range of values present in the input image [24]. Data values in the input image that are below the

14

minimum or above the maximum of the mapped range is treated the same as the minimum and

maximum, respectively. To implement windowing, the user must specify the [*low*, *high*]

intensity range in the input image they wish to display. All input pixels/voxels with intensity

values less than *low* are mapped to 0, all input pixels/voxels with intensity greater than *high* are

mapped to either 1 or 255, and all input pixels/voxels with values in the range [*low*, *high*] are

mapped to output values using the following: $f'(y, x) = \frac{f(y,x) - low}{high - low} * (255)$. Generally speaking,

narrower window width gives higher contrast. This simple operation can either be performed by

our C++ program using the scale function given previously after thresholding the minimum and

maximum values, or it can be done interactively in *MeVisLab*. Figure 3.3 shows the user

interface in which window position and width can be manually set by sliding the black and white

marker points on the greyscale. The desired window position and width depends on the particular

image being displayed and region of interest (ROI) in that image. This functionality is especially

helpful in analyzing different slices in time domain since raw floating point pixel/voxel values

have a much wider range than typical greyscale range. For most of our samples, we commonly

pick a window that is centered on the major peak in the histogram of the displayed image.

Automatic windowing that exploit image statistics is deferred to future work to enable faster
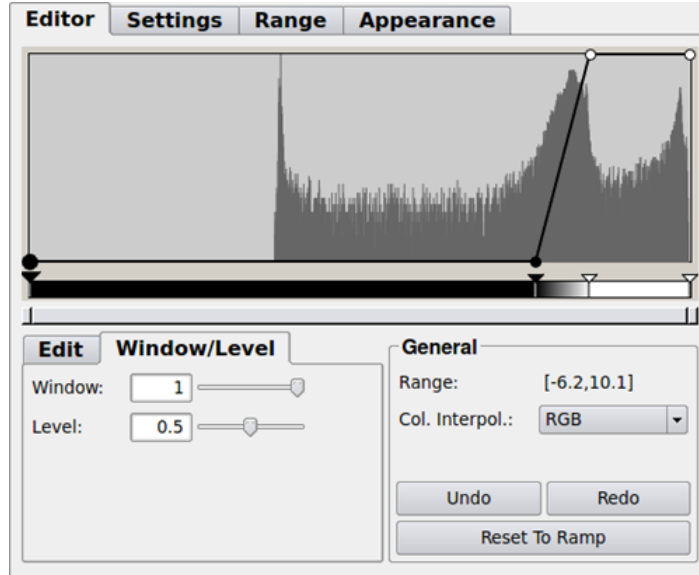
visualization.

Figure 3.3: Graphical user interface in *MeVisLab* that allows for manual windowing adjustment of displayed intensity. By sliding the black and white marker points below the histogram, various window position and width can be specified that result in displayed images of different brightness and contrast.

Histogram Equalization

Histogram equalization is a classical image processing technique used to increase the overall contrast of an image [24][25]. It enhances image contrast by spreading out pixel intensities that are distributed in a narrow range in the input image into a broader intensity range. This desired transformation is usually implemented by calculating cumulative distribution function of pixel intensities in the input image with L possible intensity levels (i.e. 256 for an 8-bit image), that is, $cdf(r_k) = \frac{1}{MN} \sum_{j=0}^{k} n^j$, where $k = 0, 1, 2, \dots, L-1$, MN gives the total number of pixels in the image of size $M \times N$, and n^j is the number of pixels with intensity value r_j [24]. A pixel with intensity value r_k in the input image is then mapped to the output pixel value s_k by the following equation: $s_k = T(r_k) = \frac{(L-1)}{MN} \sum_{j=0}^{k} n^j$. Histogram equalization is commonly implemented in most of existing image processing software. We used a built-in module in *MeVisLab* to perform histogram equalization on our sample data.

16

Unsharp Masking

Unsharp Masking is a classic linear image enhancement technique [24]. An unsharp (smoothed) version of the original image is first subtracted from the original image to obtain a mask. Output image pixels are then calculated by adding a weighted portion of the mask back to the original image. In other words, $mask(y, x, t) = input(y, x, t) - blurred(y, x, t)$, and $output(y, x, t) = input(y, x, t) + alpha * mask(y, x, t)$, where $alpha > 0$ is usually some small constant. The amount of enhancement applied is controlled by varying the weight alpha as well as the amount of blurring in the mask image, which is controlled by the size of the blurring neighborhood used to create the mask. Local averaging and Gaussian blurring are two common ways used to create the blurred masks. We experimented with both methods and overall little difference in the output images was noticed between them. For simplicity, we used local averaging to explore how varying alpha value and amount of blurring in the mask image affect the enhancement. We also varied the shape of the blurring neighborhood to see how blurring in the spatial and time domain have different effects on the enhancement.

Figure 3.4 shows the processing pipeline in *MeVisLab* that implements unsharp masking. In this user interface, nodes represent image processing modules, and edges connecting nodes indicate the order in which operations are performed. Images are first loaded in with a module called *imageload*. Then to create the unsharp mask, a *convolution* module is used that takes a user defined convolution filter, such as an averaging kernel, in the module *kernelEditor* to generate the blurred image, and then subtract it from the original image. Image arithmetic is handled by the *arithmetic* modules, and final output image is obtained by adding a weighted potion of the mask to the original image and displayed in the *orthoview2D* module.
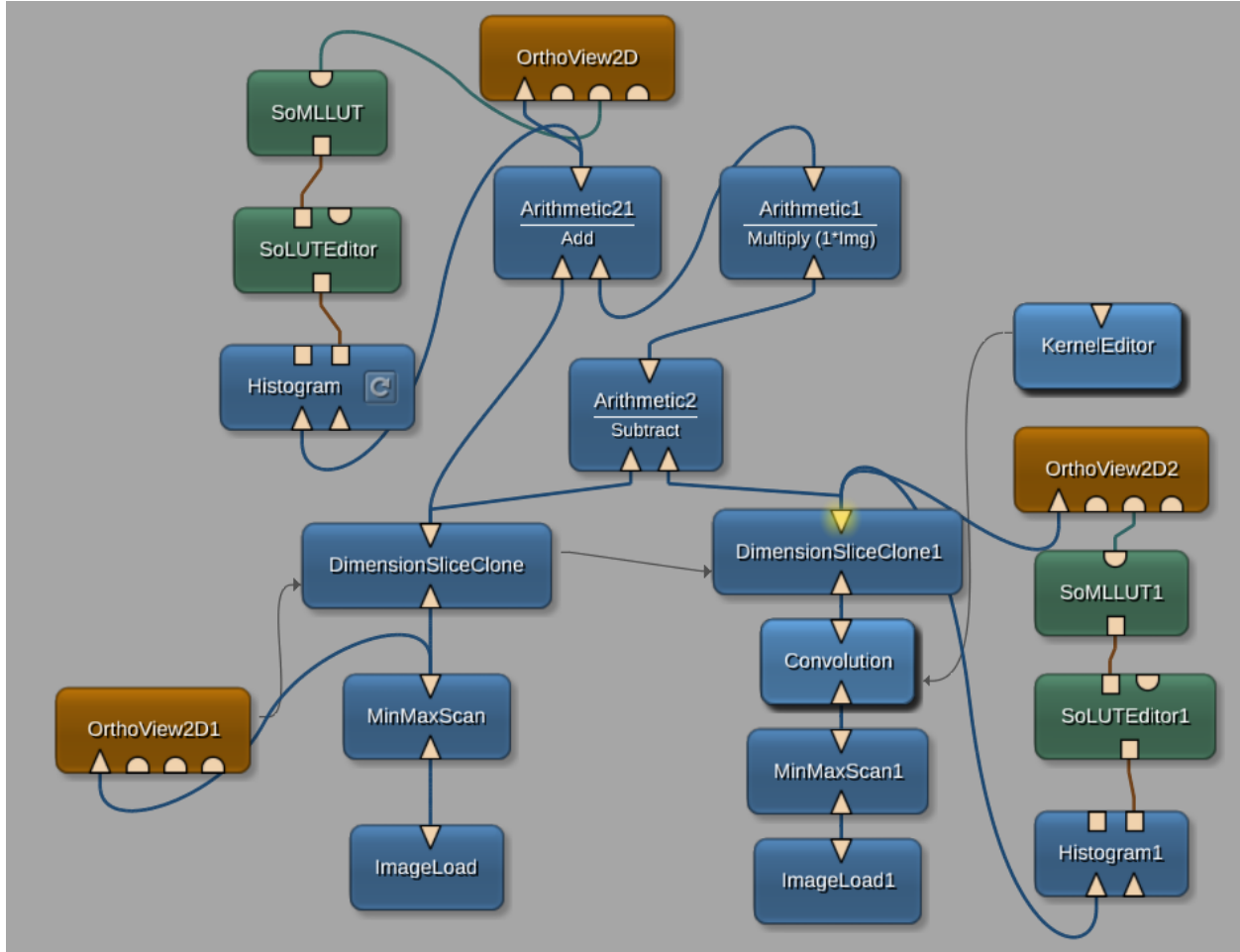
Figure 3.4: Unsharp masking implemented in *MeVisLab*. Modules that perform relevant tasks are connected to form a processing pipeline that takes an input image and produces an output image.

Laplacian Sharpening

Laplacian sharpening is another common enhancement method that increases the visibility of small details in an image [24]. The Laplacian operator, which is really a discrete formulation of the second-order derivative in an image, is defined at a specific image pixel as:

$$\nabla^2 f = \frac{\partial^2 f}{\partial x^2} + \frac{\partial^2 f}{\partial y^2}, \text{ where}$$

$$\frac{\partial^2 f}{\partial x^2}(x,y) = f(x+1,y) + f(x-1,y) - 2f(x,y), \text{ and}$$

$$\frac{\partial^2 f}{\partial y^2}(x,y) = f(x,y+1) + f(x,y-1) - 2f(x,y)$$

This linear second-order derivative operation can be represented by several 3x3 convolution kernels, depending on whether diagonal pixels are considered. The two kernels we used in our experiments are the following:

0	-1	0		-1	-1	-1
-1	4	-1		-1	8	-1
0	-1	0		-1	-1	-1

Figure 3.5: Filter kernels used to generate the Laplacian masks in our experiments. The kernel on the left corresponds to the discrete Laplacian equation above. The kernel on the right corresponds to an average of the discrete Laplacian taken along the x and y axis with the Laplacian taken along the two diagonal directions.

The Laplacian image is obtained by convolving one of the kernel masks as shown in Figure 3.5 with the original image. Because Laplacian is a second-order derivative operator, it highlights intensity discontinuities in an image and deemphasizes regions with slowly varying intensity levels. The sharpened output image is obtained by adding the Laplacian image back to the original image, just as in unsharp masking. That is, $output(y, x, t) = input(y, x, t) + alpha * Laplacian(y, x, t)$. We tested how the amount of enhancement is affected by the alpha value for each of the Laplacian kernels shown above.

<u>Statistical Differencing</u>

Statistical differencing is a nonlinear image enhancement technique that increases the visibility of fine details in an image by adjusting pixel intensities based on local statistical properties of an image [25]. In particular, output images O are calculated using the following:

$$O(y, x, t) = \frac{I(y, x, t) - m(y, x, t)}{s(y, x, t)}$$

In this case, $m(y, x, t)$ is a local estimate of the mean, and $s(y, x, t)$ is a local estimate of the standard deviation, both in a neighborhood centered at (y, x, t) in the input image I. The amount of contrast enhancement that is performed is determined by the size and shape of the neighborhood used to calculate the local statistics. Smaller neighborhoods provide more image enhancement and larger neighborhoods result in less enhancement.

D.   Image Segmentation

Edge Detection

Edge detection is of particular interest in this work since one of the main objectives is to determine whether positive margins are present in a given THz scanned sample. A variety of processing techniques are developed for edge detection that are based on first- and second-order derivatives of image [26]. We first experimented with applying two commonly used first-order derivative operators, Roberts cross and Sobel, to detect edges in our images that correspond to tissue boundaries. The Roberts cross operator implemented in *MeVisLab* is defined as:

$$O(y, x) = (G_1(y, x)^2 + G_2(y, x)^2)^{1/2}, \text{ where}$$

$$G_1(y, x) = f(y, x) - f(y + 1, x + 1), \text{ and}$$

$$G_2(y, x) = f(y + 1, x) - f(y, x + 1)$$

$G_1(y, x)$ and $G_2(y, x)$ can be calculated by filtering with the following two kernels in Figure 3.6.

1	0·
0	-1

0	-1
1	0

Figure 3.6: Roberts cross operators in two diagonal directions

The Sobel first derivative operators are similarly defined as:

-1	-2	-1
0	0	0
1	2	1

-1	0	1
-2	0	2
-1	0	1

Figure 3.7: Sobel operators in the y and x direction

The Sobel operator in the t direction is similar but not shown in Figure 3.7. The gradients g_x, g_y, and g_t in each of the three directions are computed by convolving the input image with each of the Sobel operators in the corresponding direction, and the final output image is calculated by summing up the magnitude of the gradients in all directions. In other words,

$$O(y, x, t) = \left|g_y(y, x, t)\right| + |g_x(y, x, t)| + |g_t(y, x, t)|$$

A main issue with these two simple gradient operators are their sensitivity to noise and fine details in input image [26]. To be able to detect the principle edges that surround regions of cancer in our THz images while resisting the small intensity fluctuations commonly present inside fibroglandular tissue areas, smoothing is used prior to applying the gradient operators and the resulting gradient magnitude images are further thresholded to only display the strong edges.

Besides these two simple first-order derivative operators, we also experimented with a more advanced technique called the Canny edge detector [27]. Although complex and computationally intensive, the Canny edge detector is usually superior in terms of effectiveness than most other simple edge detectors [26]. It was designed around three performance criteria [27]: "1) Good detection. There should be a low probability of failing to mark real edge points, and low probability of falsely marking non-edge points. 2) Good localization. The points marked as edge points by the operator should be as close as possible to the center of the true edge. 3)

Only one response to a single edge." The algorithm consists of four major steps, which can be summarized as following [26]: "1) Smooth the input image with a Gaussian filter. 2) Compute the gradient magnitude and angle images. 3) Apply nonmaxima suppression to the gradient magnitude image. 4) Use double thresholding and connectivity analysis to detect and link edges." For a detailed discussion on the exact calculation and implementation, interested readers are deferred to the original paper [27] as well as other third-party references [26][28]. For our experimentation, we used an open-source implementation from the *Insight Segmentation and Registration Toolkit (ITK)* [29], which has been encapsulated as a module in *MeVisLab*. We tested it on two of our dataset with different input parameters.

Region Growing

Region growing is another common image segmentation method [26]. As the name suggests, it is a process in which we group pixels into larger regions by expanding from already identified smaller regions based on some predefined criteria. This approach leverages inherent similarities that exist between pixels that belong to the same region. The criteria for expansion usually depend on the problem and image data available. In our case, we considered two criteria for expansion and evaluated the effectiveness of each approach. To get the growing procedure started, seed points must be specified from which regions will grow. Neighboring pixels of the seed points that satisfy the predefined constraint will be included with the seed points to form a larger region. One approach is that the pixels at the boundaries of the identified regions will then act as new seed points from which we try to expand the regions further. Another approach is that candidate pixels adjacent to the border of identified regions compare only with the initial assigned seed points to whose region they will be included into. In either case, this recursive procedure continues until either when no more neighboring pixels can be included into the

existing regions or when image border is encountered. When the procedure stops, we have then segmented the image into its constituent parts.

This simplest expansion criterion is defined by thresholding pixel intensities. We define the distance d between two neighboring pixels as the absolute value of their intensity difference, and we group them into the same region if $d < threshold$ for some predefined $threshold$. While this approach is universal for all types of images and is the simplest to implement, it has several drawbacks as will be shown in our evaluation.

To better utilize the time-domain measurement we obtained in our THz images, we need to consider a sequence of data points in a waveform rather than just picking a single point from it. The sequence of data values at a given spatial location within a time range can be treated as a vector of dimension n, where n is the number of data points in that time range. This allows us to calculate a difference vector between two pixels that span the same length in time domain. We can then define the distance between the two pixels as the norm of the calculated difference vector. We experimented with *L2* norm and evaluated its performance. One reason that we think *L2* norm will work well is that the recorded data values in time domain between tissue regions and cancer regions show significant distinction. This can be best seen in Figure 3.8. The plot shows three time series that correspond to three pixel locations in one of our THz images, each one picked arbitrarily from the inside of regions that correspond to healthy tissue, tumor, and paraffin-covered glass slide. It is easily seen that the THz response curves between the fibro tissue and cancer region show a significant dissimilarity that can be exploited in our region growing. Specifically, while the response curve of the tumor region is characterized by a major negative peak, followed by a major positive peak, and then a minor negative peak, the response curve of the fibro region has two positive peaks in between the initial and final negative peaks.

Not only does the fibro region show four noticeable peaks instead of three, each of these peaks exhibits considerably less amplitude than the peaks shown by the response curve from the tumor region. The locations of the peaks with respect to time also differ in the two regions. The three peaks of the cancer response curve reside in a narrower time range than the four peaks of the fibro response curve. All these distinctions will contribute to the *L2* norm in the distance calculations during the execution of our region growing procedure. The distinction between these response curves can also be easily seen in the time domain side views on the right of Figure 3.9. The top right view corresponds to the horizontal scanline in the bottom left view, and the bottom right view corresponds to the vertical scanline in the bottom left view. Notice how different regions show drastically distinct patterns in the time domain.
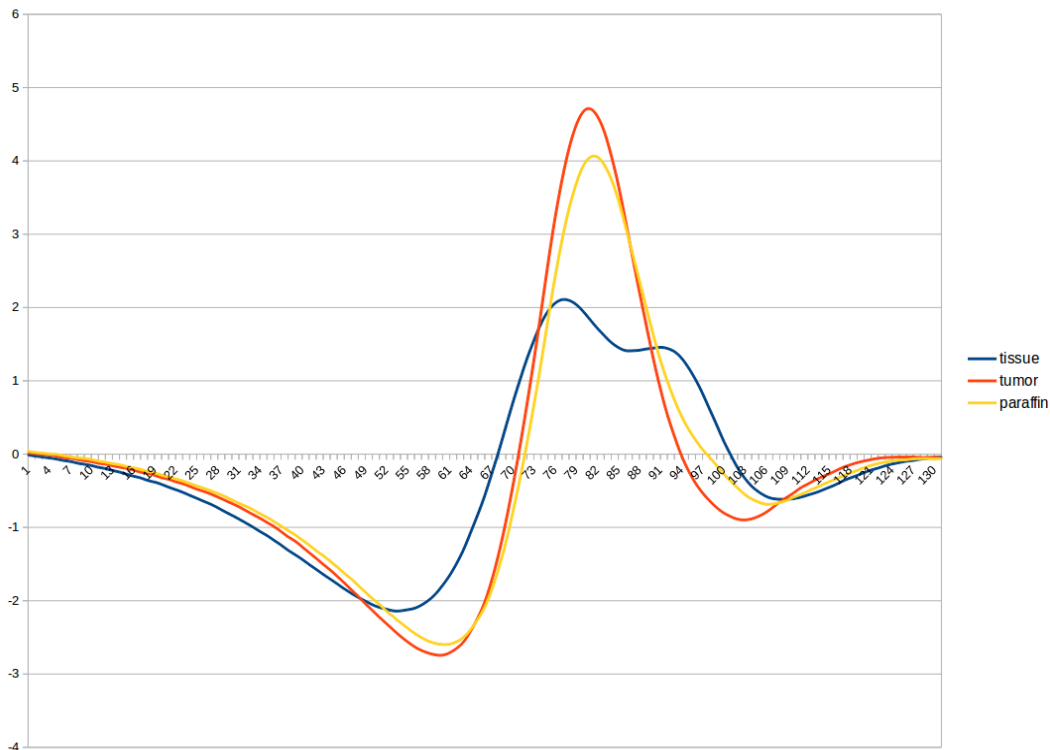
Figure 3.8: The typical THz response curve measured from the fibroglandular, tumor, and paraffin-covered glass slide regions in our dataset.
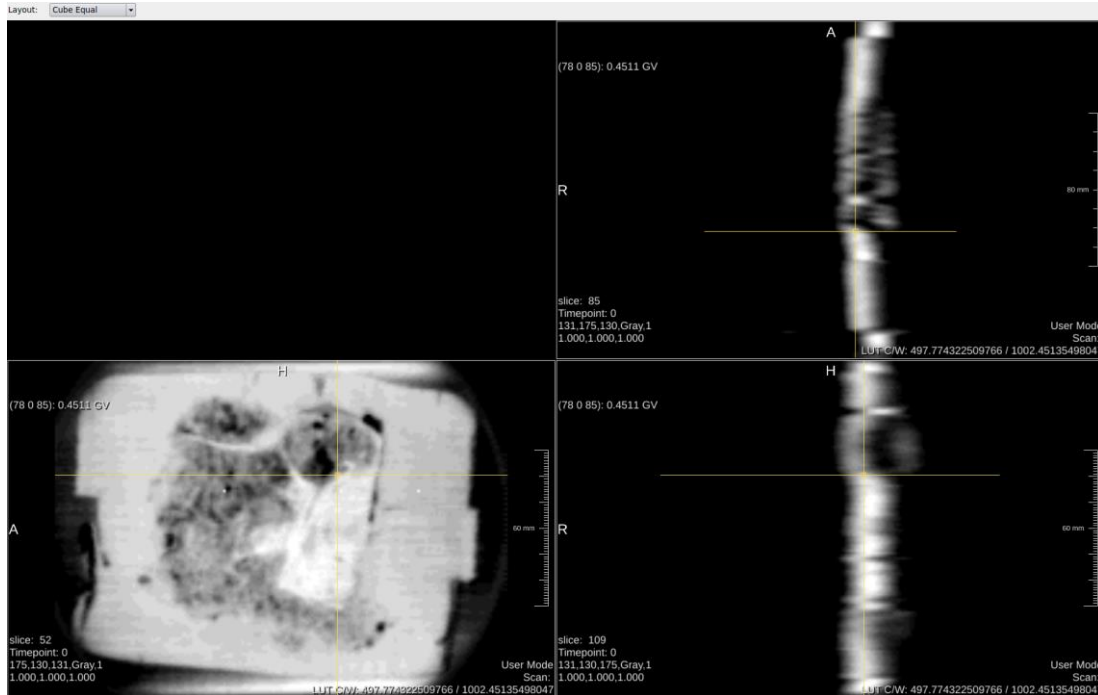
Figure 3.9: Time-domain side views at a tissue/tumor boundary point as visualized in *MeVisLab*.

E. Block Scan Enhancement and Visualization

The discussion so far have been focused solely on THz scans of sliced samples with thicknesses of 10μm to 30μm. These thin slices were cut from whole tissue blocks that were purchased from different biobanks, as mentioned previously. Pulsed THz scans of these whole tissue blocks were also obtained in reflection mode prior to preparing the sample slices. Similar techniques as those used for sliced scans can be applied to enhance and visualize block scans. Some of our results are shown in the Results and Evaluation section below.

F. Volume Visualization

Since our THz scanned data are three dimensional in nature, we also explored how volume rendering can help us visualize the samples. Volume rendering is a computer graphics technique that was invented to help visualize 3D structures within medical images [30]. The basic idea is to treat edges within the volume as surface elements, and calculate how a synthetic

light source would reflect off these surfaces when viewing the volume from different angles. By selecting what edges are of interest, users can gain an understanding of the size, shape and orientation of structures within medical images. For example, for CT images, it is possible to view edges between tissue and bone to understand the geometry of bones, or the edges between air and tissue to understand the geometry of tissue. By making these two surfaces semi-transparent, it is also possible to visualize bones and tissues simultaneously. This is illustrated in Figure 3.10 where the four surfaces corresponding to muscle, fat, bone, and blood in a CT image of a forearm are volume rendered together.
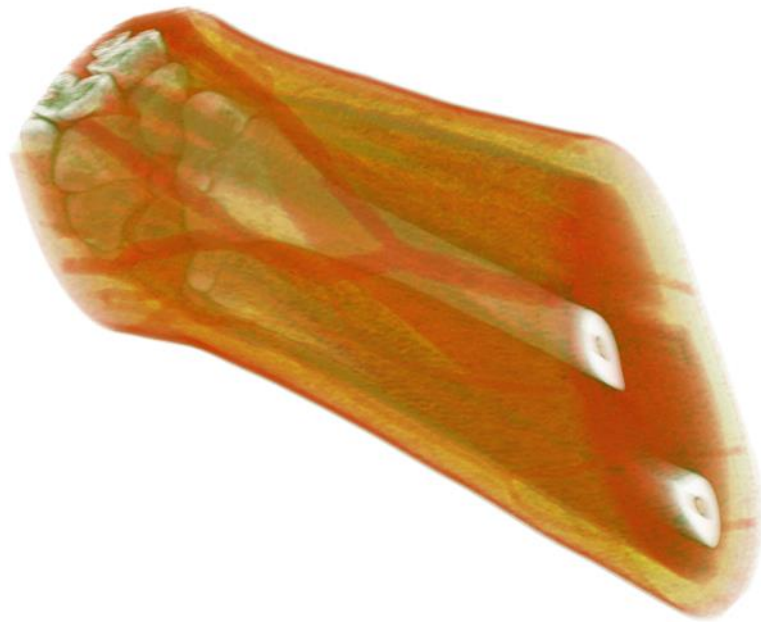
Figure 3.10: Volume rendered CT scan of a forearm with different color schemes for muscle, fat, bone, and blood (from Wikipedia [31]).

MeVisLab has a built-in volume rendering module that we can use to perform 3D visualization. A summary of our results using the *MeVisLab* module on 3D THz images are shown in the Results and Evaluation section below.

IV.   Results and Evaluation

A.   Image Enhancement

Scanline Registration

Scanline registration is usually the first processing step we perform on any of our dataset after reading in the raw data from TVL file since all the THz images we obtained exhibit this kind of row misalignment. Figure 4.1 and Figure 4.2 show our results of performing scanline registration using MSE on two of our datasets. The images on the left of both figures clearly show the misaligned rows throughout the entire image. All the vertical edges are corrupted by zig-zag patterns that are possibly due to the physically instable motor that drove the movable stage during the imaging process of our samples. By shifting each of the odd rows adaptively by within 3 pixels in the horizontal direction that gives the MSE with its adjacent even rows, we can significantly reduce the "saw tooth" appearance of our raw images.
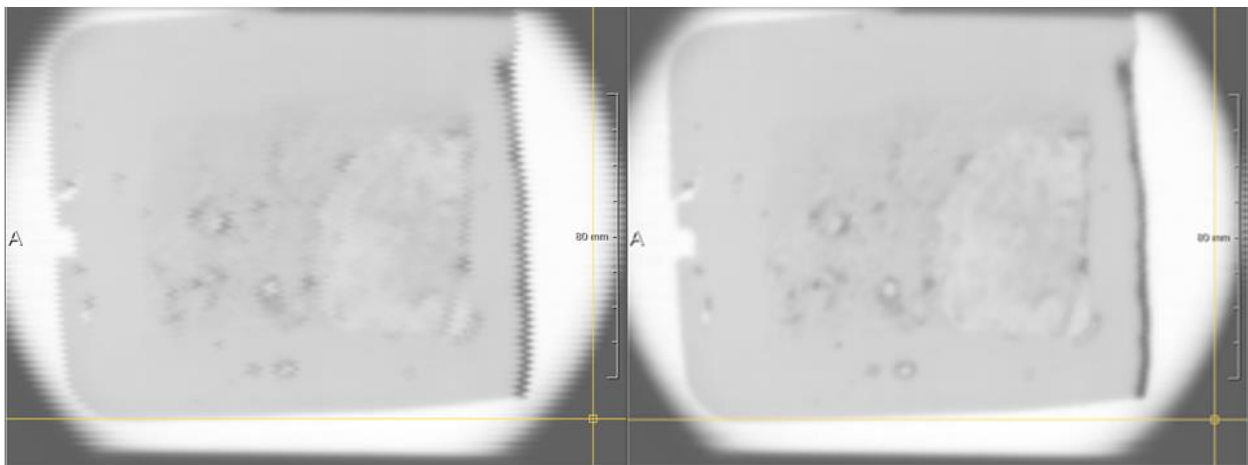
Figure 4.1: The result of applying scanline registration using MSE to one of our THz slice scans. The image on the left is the raw data with misaligned rows and the image on the right shows the correction made by applying scanline registration.
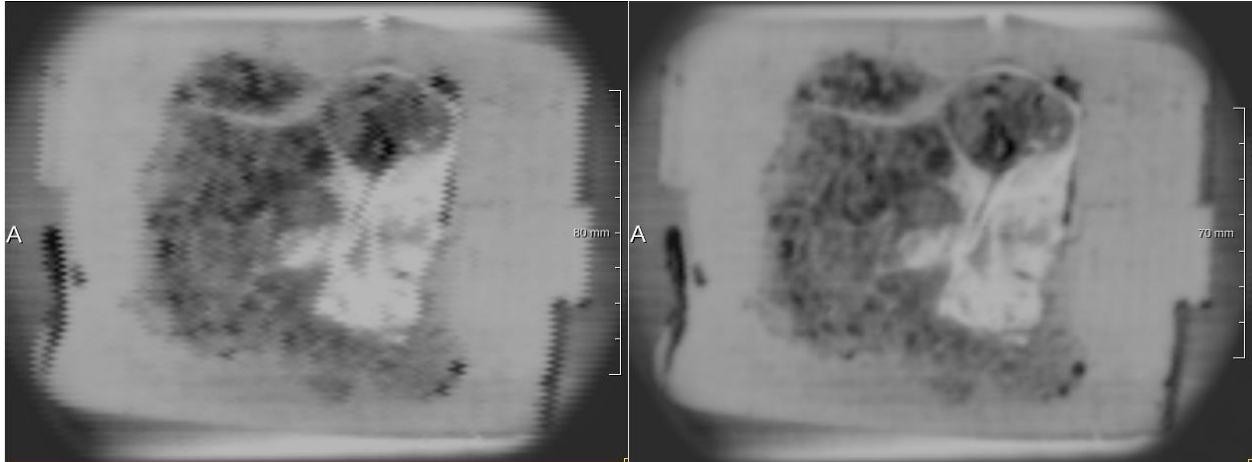
Figure 4.2: Another example of applying scanline registration using MSE to a different THz slice scan.

Intensity Windowing

Intensity windowing is applied to our sample data to generate images with a lot more discernable details. Figure 4.3 shows its result when applied to one of our tissue slice images. The top left image is displayed without intensity windowing. The other three images are displayed with decreasing window width. The bottom right image has the smallest window width and thus the most contrast. Tissue structure and tumor are clearly more identifiable in the windowed images than in the raw input image. Figure 4.4 and 4.5 show two other examples of how intensity windowing can substantially increase the visibility of our imaged samples. The enhanced images on the right side are able to reveal a lot more details in the scanned samples than the displayed raw images shown on the left in each of the two figures. Notice that both figures are scans of slices that were cut from the same tissue block. Figure 4.4 was imaged in reflection mode, and Figure 4.5 was imaged in transmission mode. A much narrower window width is used for the transmission image than the reflection image in this case, although we do not have enough samples currently to show that this is true in general.
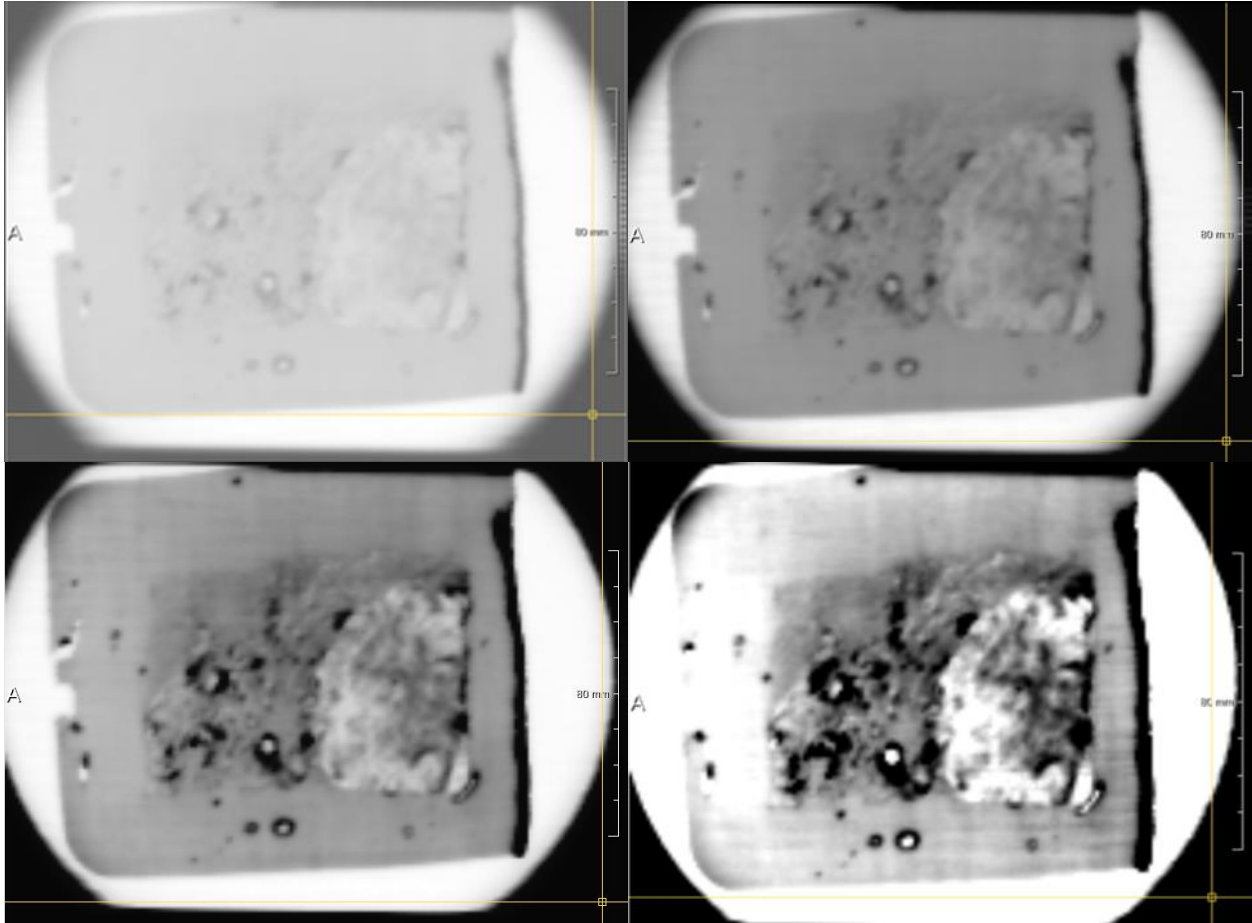
Figure 4.3: Application of intensity windowing to a tissue slice image obtained in reflection mode.
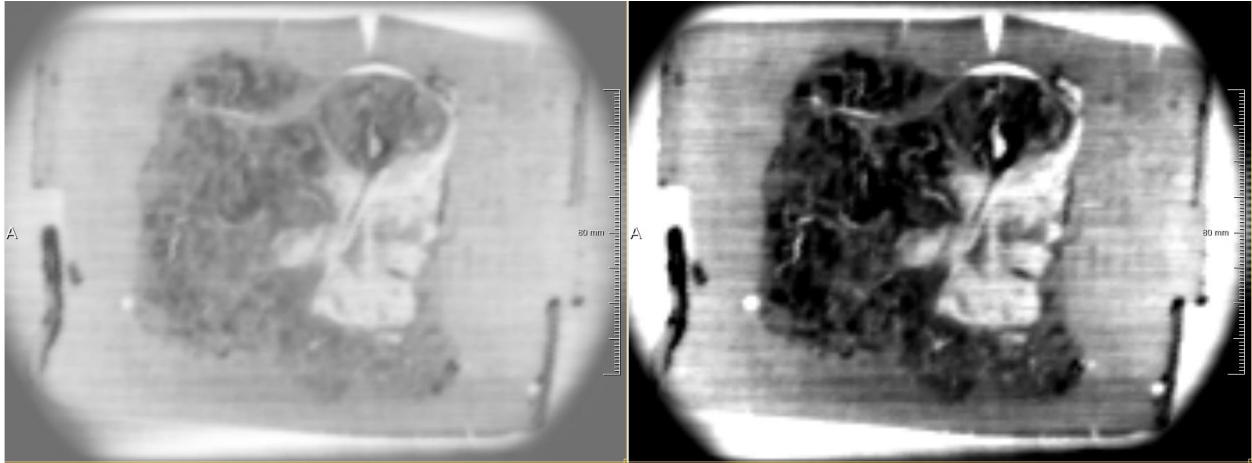
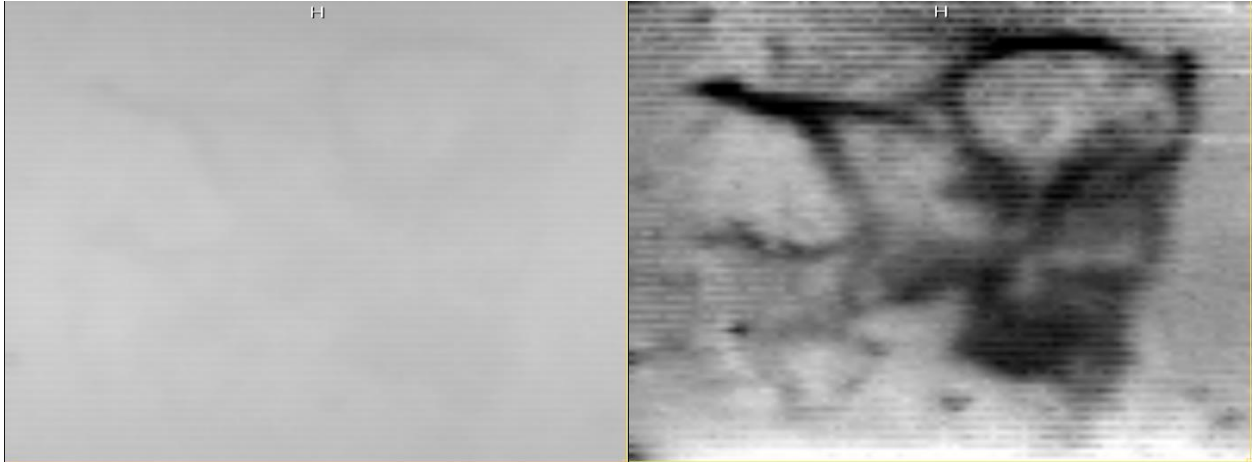Figure 4.4: Application of intensity windowing to another tissue slice image obtained in reflection mode.

Figure 4.5: Application of intensity windowing to a slice image of the same tissue sample as Figure 4.4 obtained in transmission mode.

Histogram Equalization

Histogram equalization is used to automatically adjust the contrast of our THz images. The results of uniform histogram equalization on the same tissue slices data as above are shown below. The advantage of this equalization process is that it does not require any user input as opposed to the manual adjustment required by intensity windowing. This simple approach, however, lacks the flexibility and specificity of intensity windowing, which can be tuned to highlight specific ROI based on local image statistics.
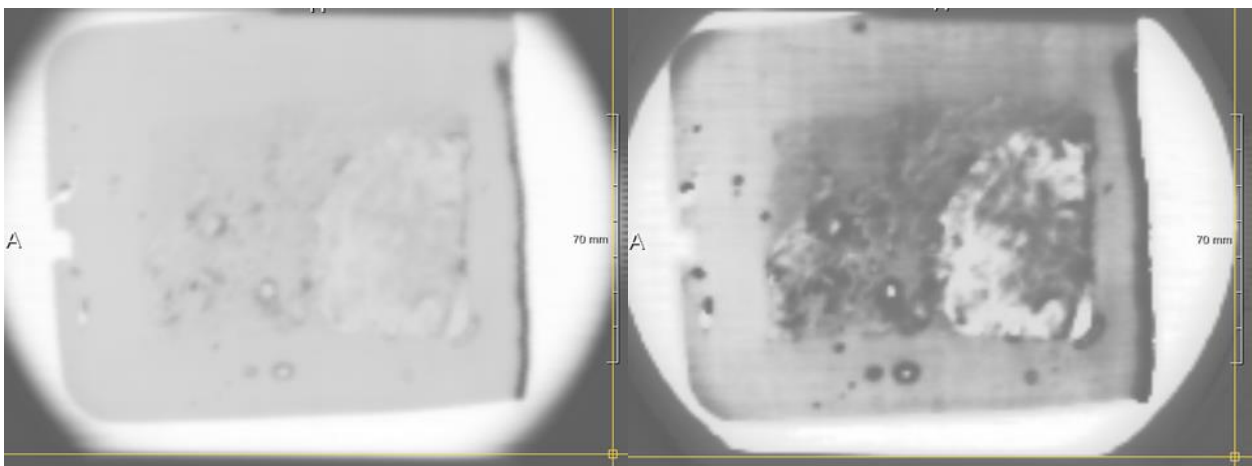
Figure 4.6: The result of applying uniform histogram equalization on the same dataset as Figure 4.3. The images on the left are the raw data displayed without histogram equalization and the images on the right are displayed after applying histogram equalization.
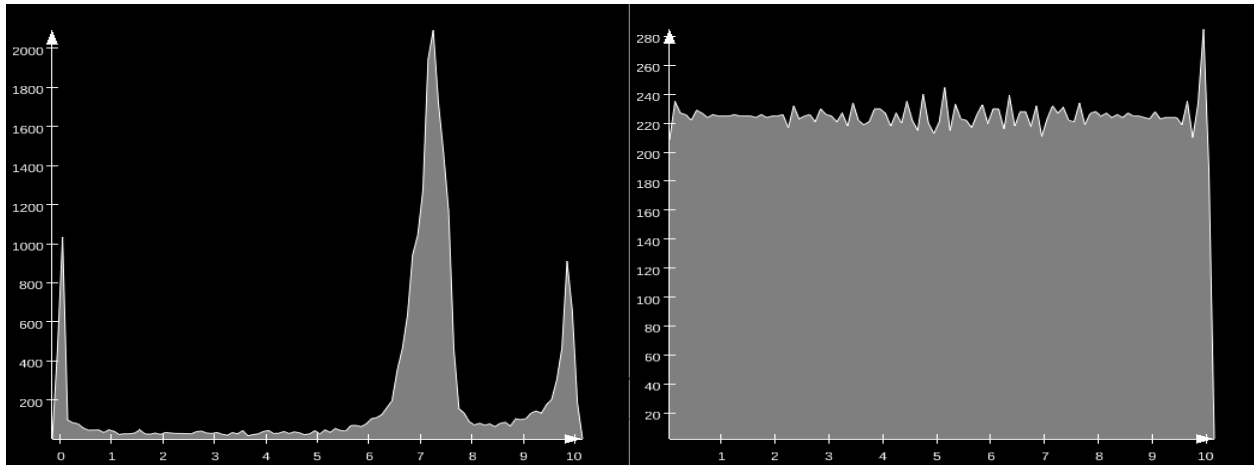
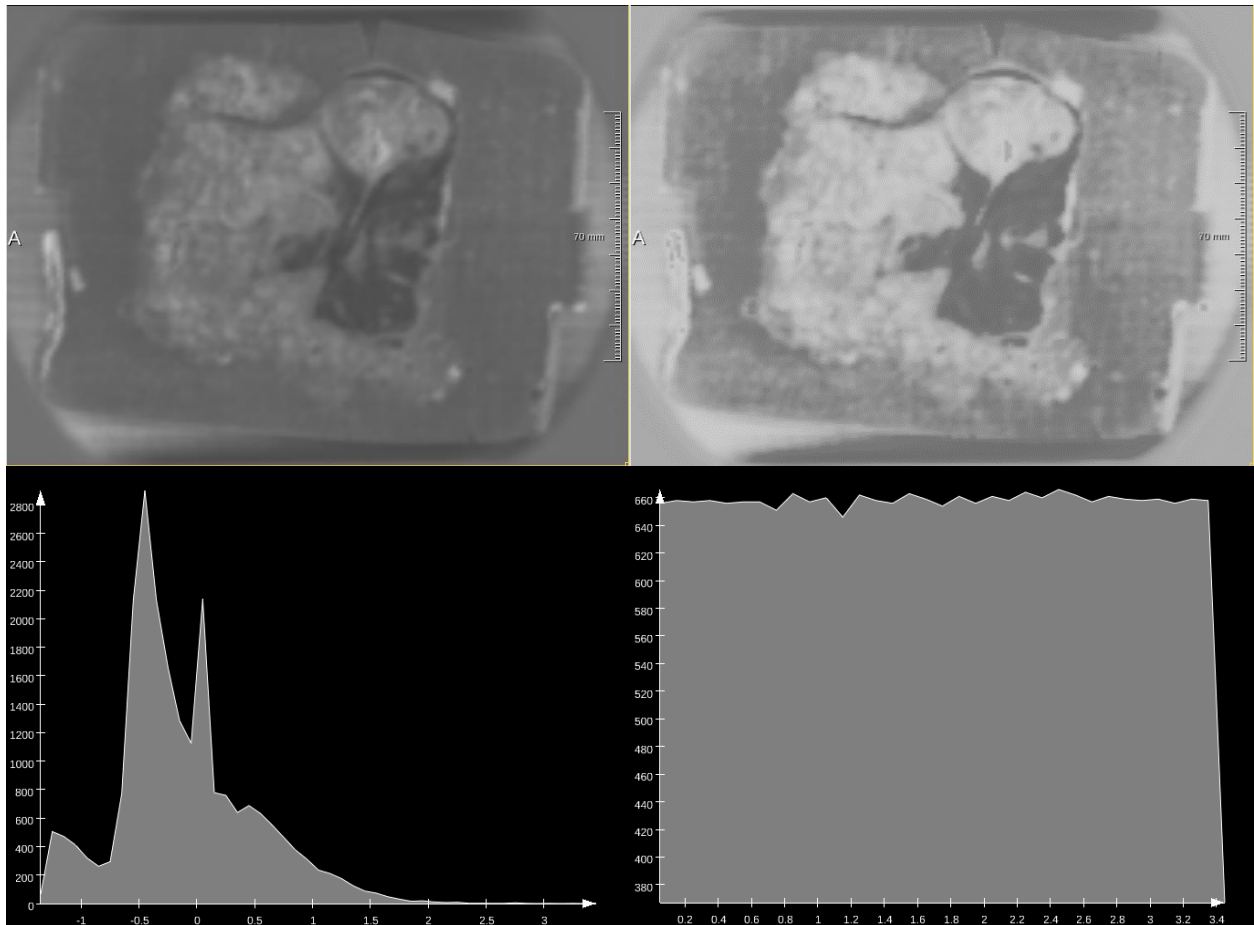Figure 4.7: The histograms of the corresponding images in Figure 4.6.

Figure 4.8: The result of applying uniform histogram equalization on the same dataset as Figure 4.4. Top row shows the raw and equalized images and bottom row shows their histograms.

Unsharp Masking

Unsharp masking is an effective method to enhance the sharpness of edges in digital images. We tested its effectiveness for our THz images with different parameters for the alpha value and with different mask images. Figure 4.9 shows the effect of different alpha values on the enhancement. As alpha increases, edges in the images appear sharper. Alpha values between 1 and 1.5 usually give satisfying enhancement. The amount of blurring in the mask image is controlled by the size of the averaging filter that is convolved with the input image to create it. Larger filter size will produce more blurring in mask image. Figure 4.10 shows the effect of different averaging filter sizes in the spatial domain that are used to create the masks. Large averaging filter sizes tend to give thickened edges. We usually choose 5x5 and 7x7 averaging filters to avoid over-enhancing. We also investigated the effect of unsharp masking applied in the one dimensional averaging window of different sizes in time domain. Unsharp masking in time domain has the effect of contrast stretching for our THz images. Higher image contrast is obtained by increasing the averaging window size while maintaining the same intensity windowing.
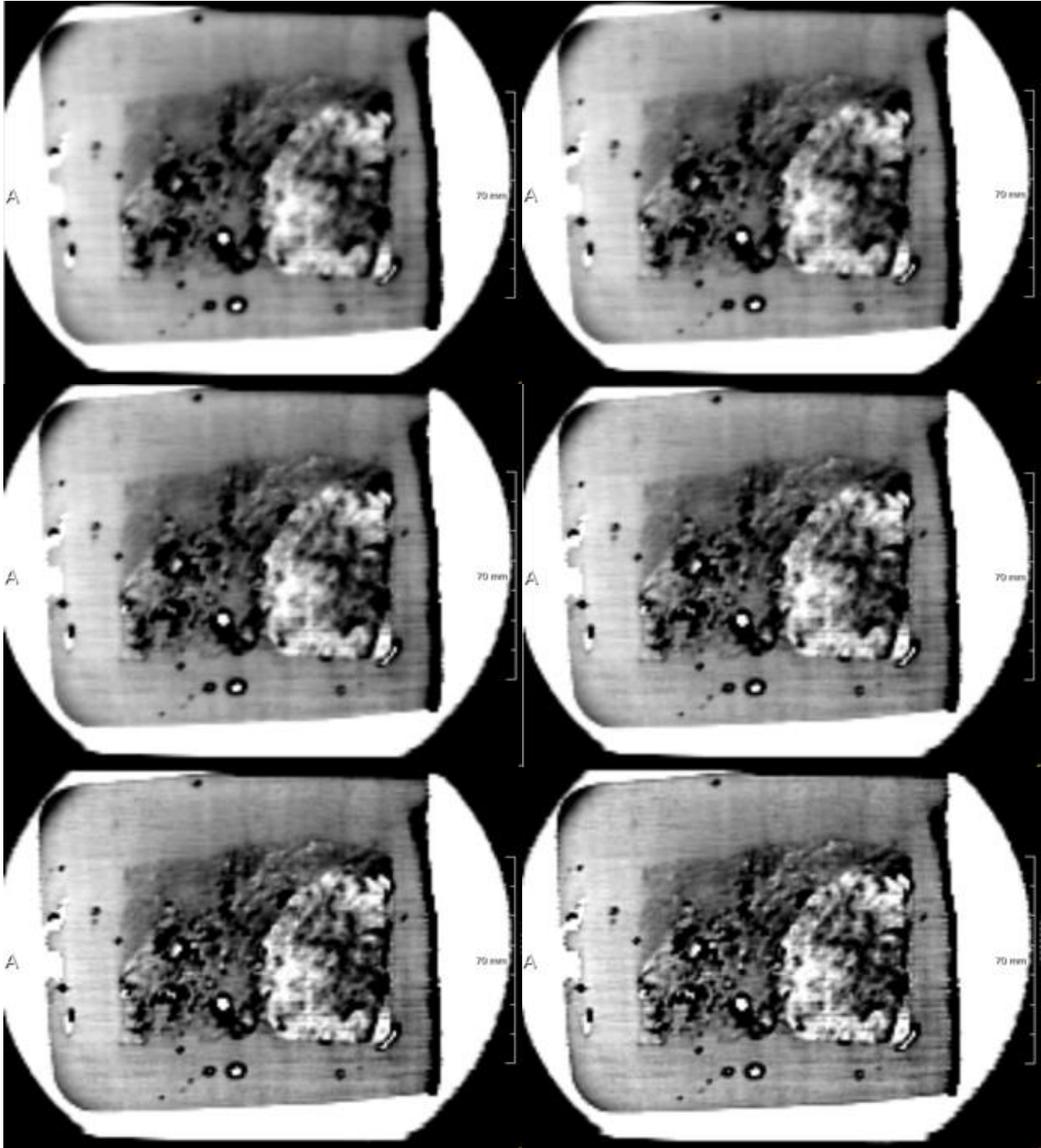
Figure 4.9: Results of applying unsharp masking with different alpha values. The left image in the first row is without unsharp masking for comparison purpose. The remaining images are displayed with increasing values of alpha, from left to right and top to bottom, with alpha equal to 0.3, 0.6, 1.0, 1.5, and 2.0, respectively.
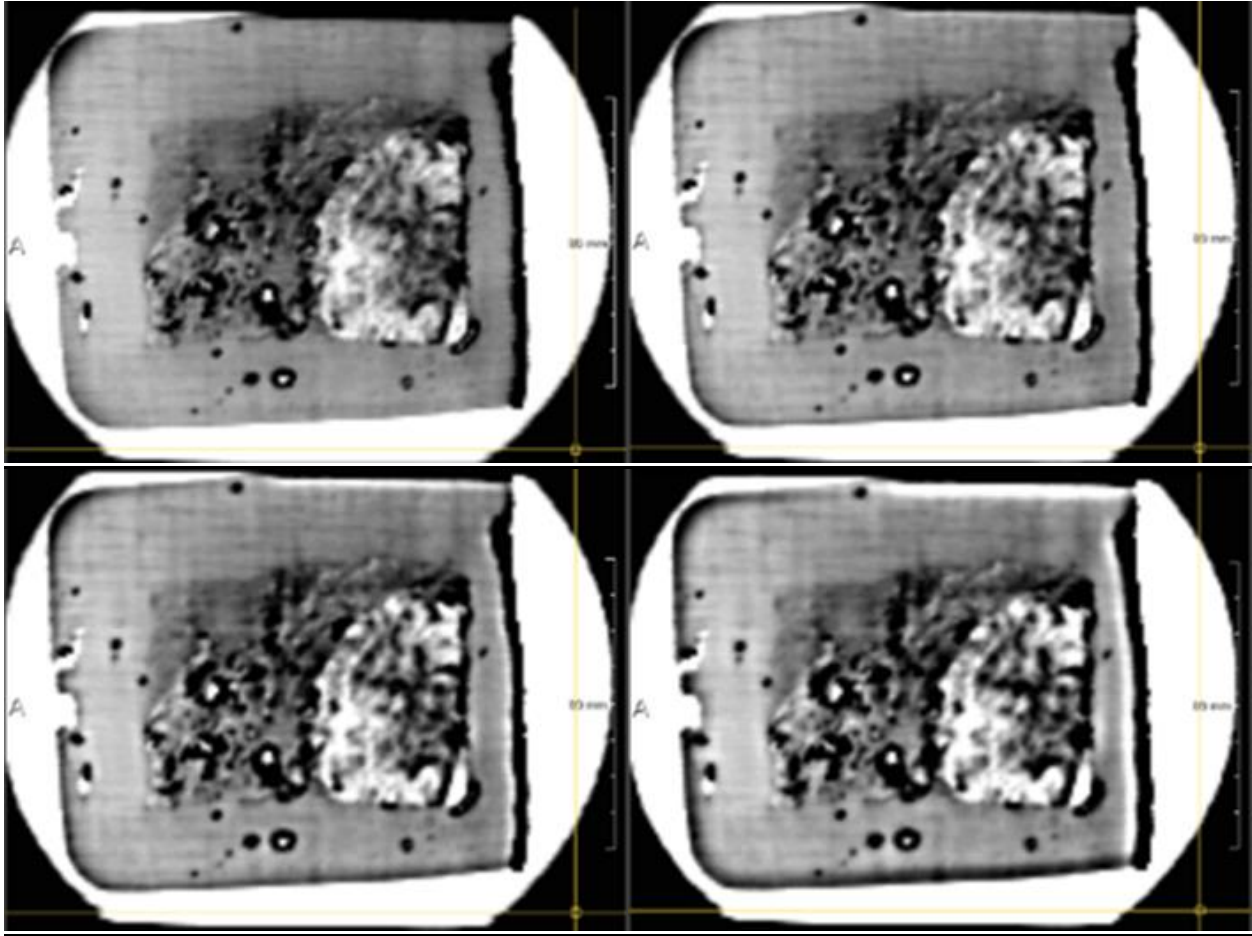
Figure 4.10: Unsharp masking images generated with different filter sizes in the spatial plane. The filter sizes used are 3x3, 5x5, 7x7, and 11x11, respectively, from left to right and top to bottom.
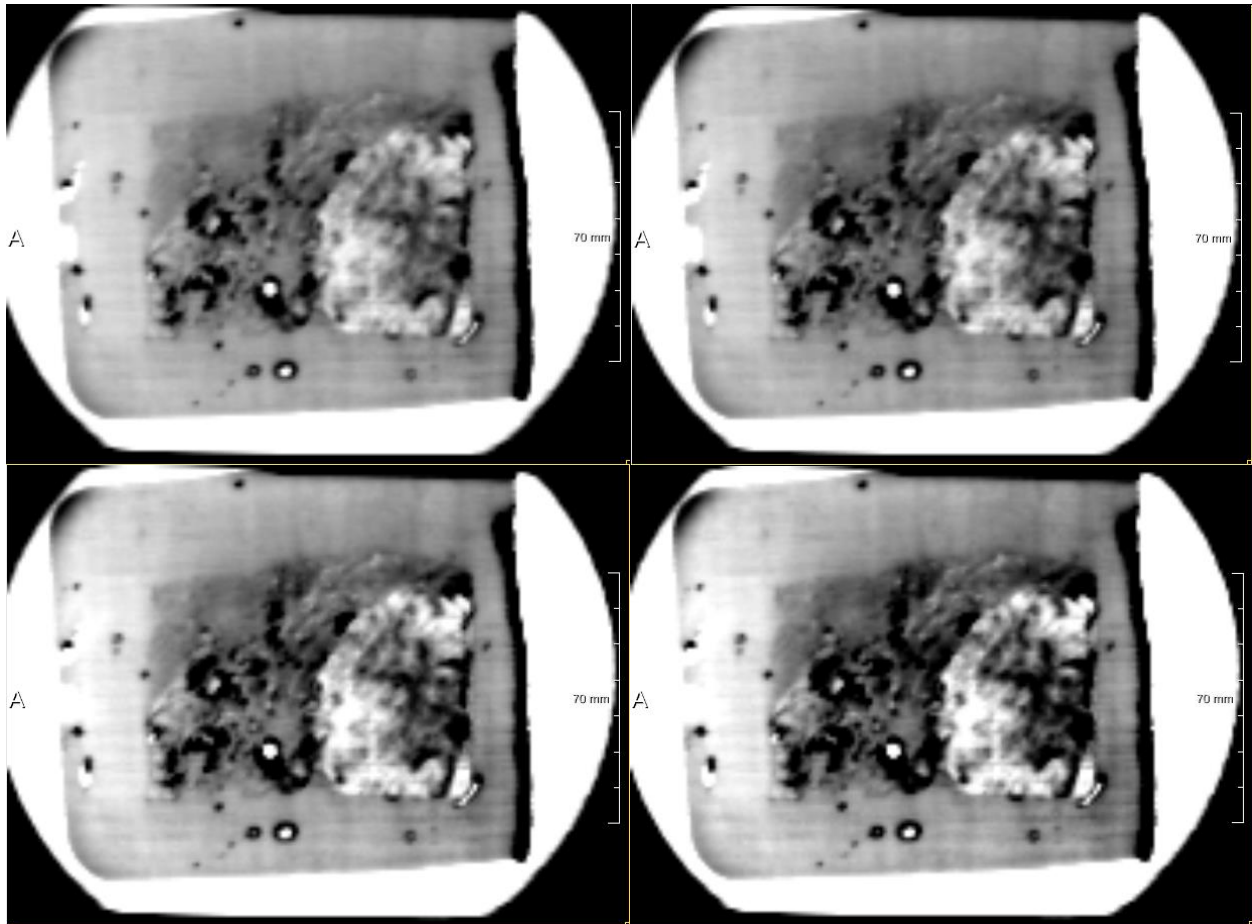
Figure 4.11: Results of unsharp masking in the time domain. Filter sizes used in the time domain are 3, 9, 15, and 21, respectively, from left to right and top to bottom.

Laplacian Sharpening

   Similar to unsharp masking, Laplacian operators can be used to create masks that

emphasize fine details in an image. In our experiments, we found that the basic Laplacian kernel

consisting of values { 0 -1 0, -1 4 -1, 0 -1 0 } (shown on the left of Figure 3.5) resulted in slightly

smoother looking output images than the rotationally invariant Laplacian kernel consisting of

values { -1 -1 -1, -1 8 -1, -1 -1 -1 } (shown on the right of Figure 3.5). We also found that alpha

values between 0.2 and 0.8 provided effective image enhancement in most images. These results

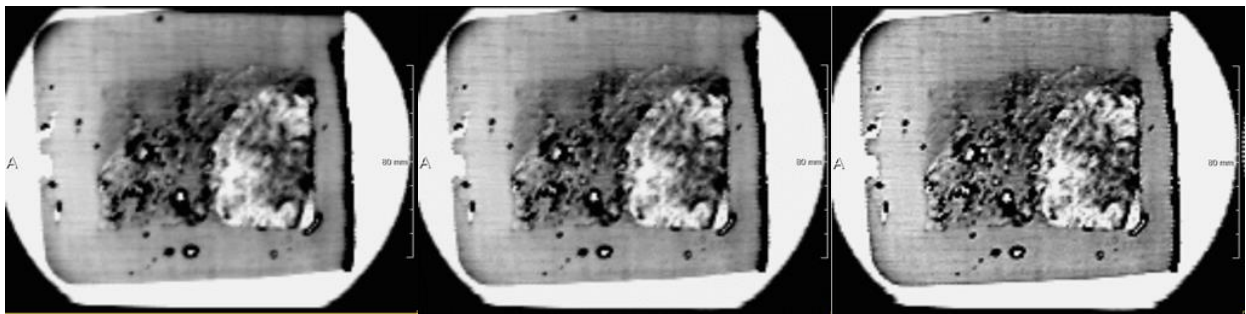are illustrated in Figures 4.12 and 4.13.

Figure 4.12: Images enhanced with the Laplacian kernel shown on the left of Figure 3.5. Alpha
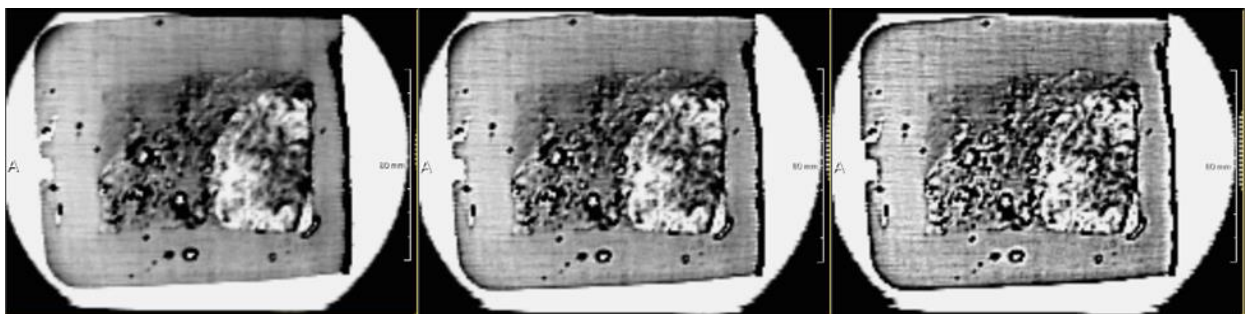values used are 0.2, 0.4, and 0.8.

Figure 4.13: Images enhanced with the Laplacian kernel shown on the right of Figure 3.5. Alpha
values used are 0.2, 0.4, and 0.8.

Statistical Differencing

   We evaluated how various neighborhood sizes and shapes affect the enhancement being

applied. Figure 4.14 shows the results of applying statistical differencing with neighborhoods of

size 3, 7, 11, and 15 in all three dimensions. Neighborhood size of $3 \times 3 \times 3$ over-enhanced the image and it is very susceptible to noise and intensity fluctuation. Larger neighborhoods in 3D give more smoothed images, but a significant loss of contrast is noticed in all cases.

We also experimented with different neighborhood sizes in the spatial and time domain. Small 2D neighborhoods in the spatial domain (3x3 and 5x5) result in noisy images with unwanted distortions, as shown in Figure 4.15. Larger neighborhoods result in less noisy images, but the original intensity variations in the images are difficult to see.

When applying statistical differencing in the time domain (Figure 4.16), however, images that show a different perspective are generated. A lot of small details are eliminated, and intensity levels seem to get reversed - what is dark in the input image gets brighter in the output image and vice versa. Tiny fluctuations in the intensity of the input image are flattened in the output image, but the major region boundaries are preserved and distinguishable.
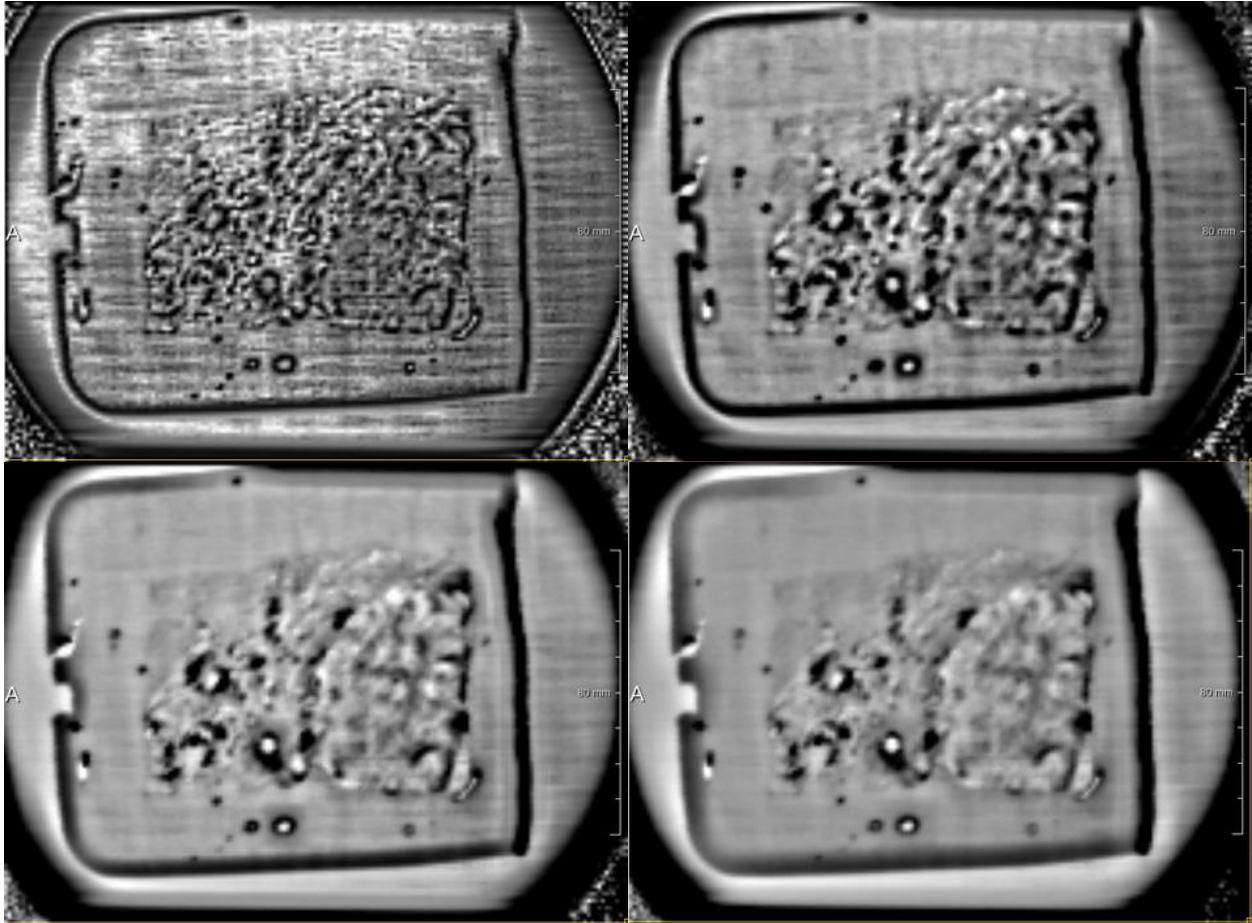
Figure 4.14: Results of applying statistical differencing with neighborhood sizes of $3 \times 3 \times 3$, $7 \times 7 \times 7$, $11 \times 11 \times 11$, and $15 \times 15 \times 15$ to one of our dataset.
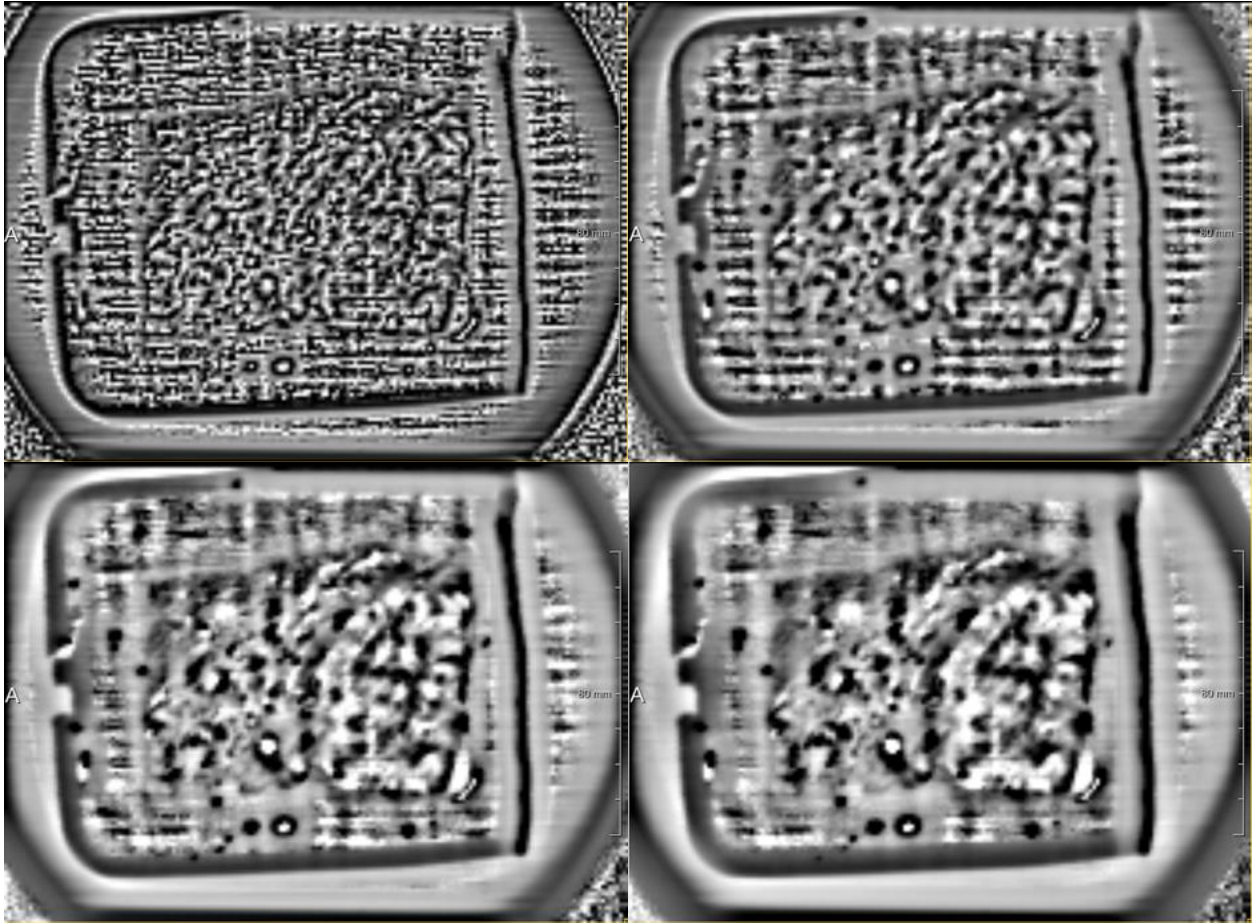
Figure 4.15: Results of applying statistical differencing with neighborhood sizes of 3 × 3, 7 × 7, 11 × 11, and 15 × 15 in the spatial domain.
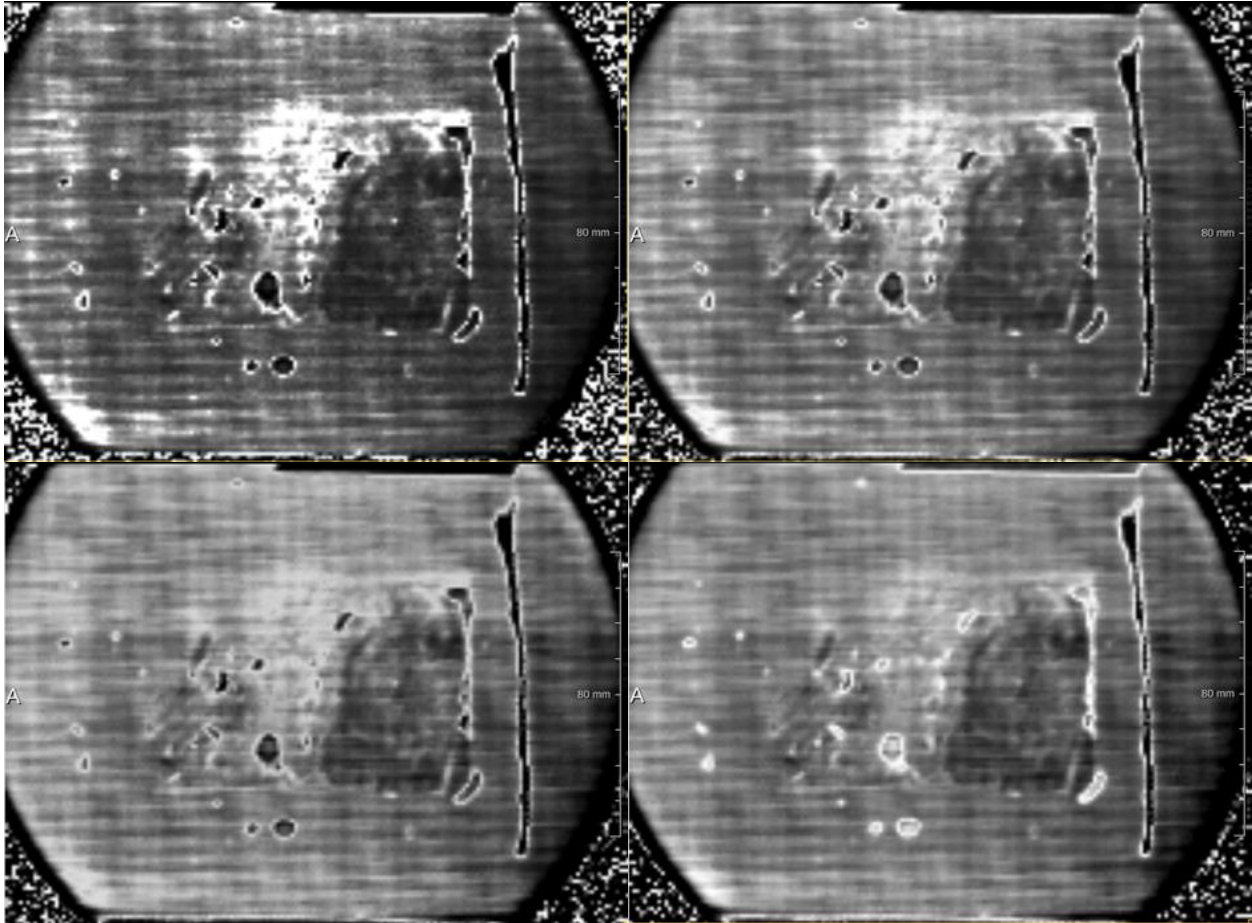
Figure 4.16: Results of applying statistical differencing with neighborhood sizes of 3, 7, 11, and 15 in the time domain.

B.   Image Segmentation

Edge Detection

We first experimented with using Roberts cross and Sobel operators to detect edges in our THz images. The results on two slice scans are shown below. From both sets of images (Figure 4.17 and 4.18), we can see that Roberts cross operator and Sobel operators have similar effect on our THz data at detecting edges. The "C" looking region on the right part of the first image set (Figure 4.17) corresponds to the region of cancer. Its general shape is outlined by the bright intensity in the processed images. The Roberts cross operator, however, seems to be more sensitive to small intensity fluctuations in this particular image. For the second set of images

(Figure 4.18), we can clearly see that the bright part on the right side of the tissue is outlined by both operators in the processed images. These detected edges signal sharp transitions in the original recorded data, which are good indicators of margins of different tissue or material regions. We do not currently have a quantified measurement of how edge intensities relate exactly to different tissue interfaces due to limited datasets we experimented with. It is a possibility that under a controlled imaging setting, edge amplitude in the gradient images can be correlated with different types of tissue interfaces so that thresholding can be employed to better aid the detection of positive margins in BCS.

Figure 4.17 shows the results of applying Roberts cross and Sobel operators on one of our dataset. The top left image is the original image displayed after intensity windowing. The top right image is generated when Roberts cross operator is applied to the original image. The images on the bottom row are generated using Sobel operators. 2D Sobel operator in the spatial domain is used for the left image, and 3D Sobel operator is used for the right image. Similarly, Figure 4.18 shows the results of applying Roberts cross and Sobel operators on another dataset.
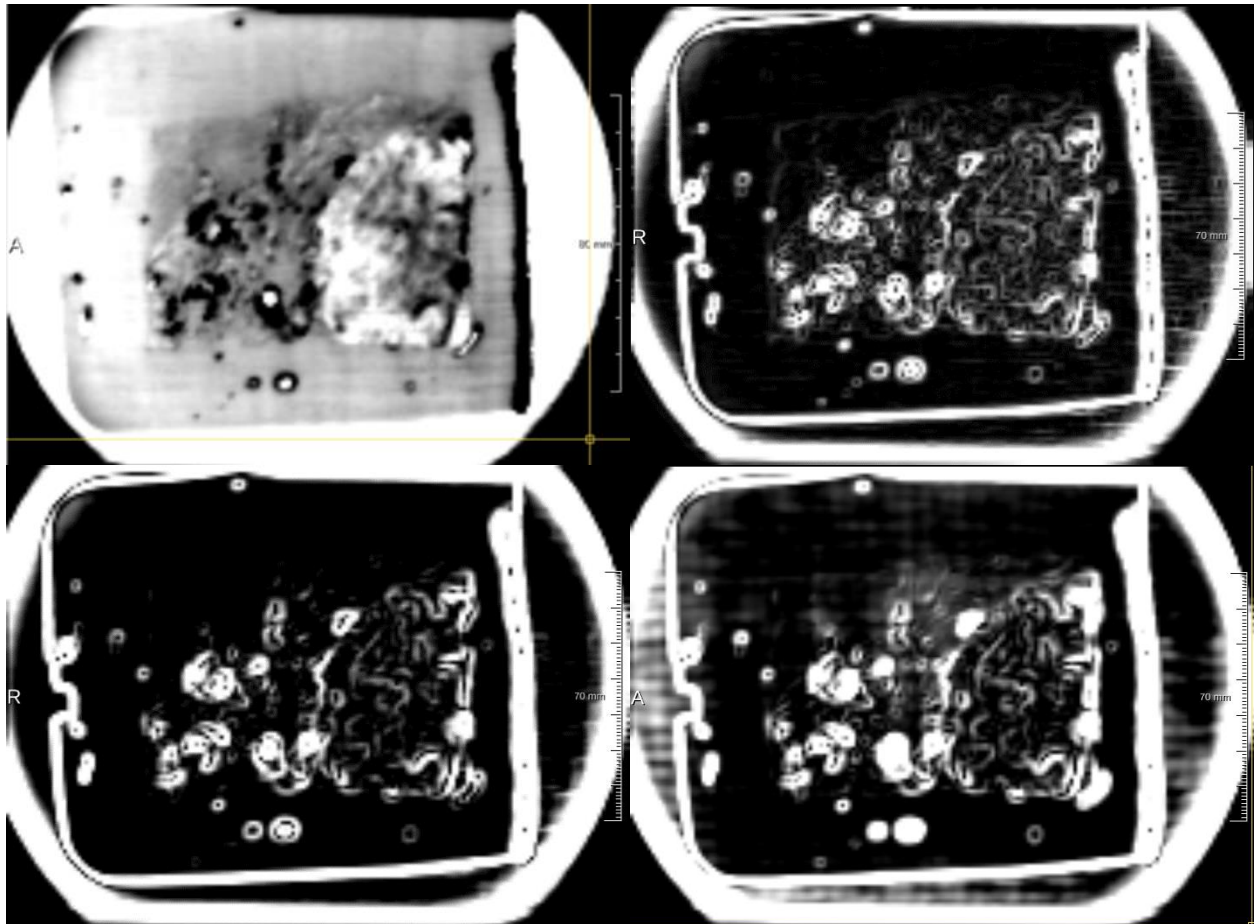
Figure 4.17: The results of applying Roberts cross and Sobel operators on one dataset. The top left image is the windowed input image, top right is Roberts cross, bottom left is 2D Sobel operator, and bottom right is 3D Sobel operator.
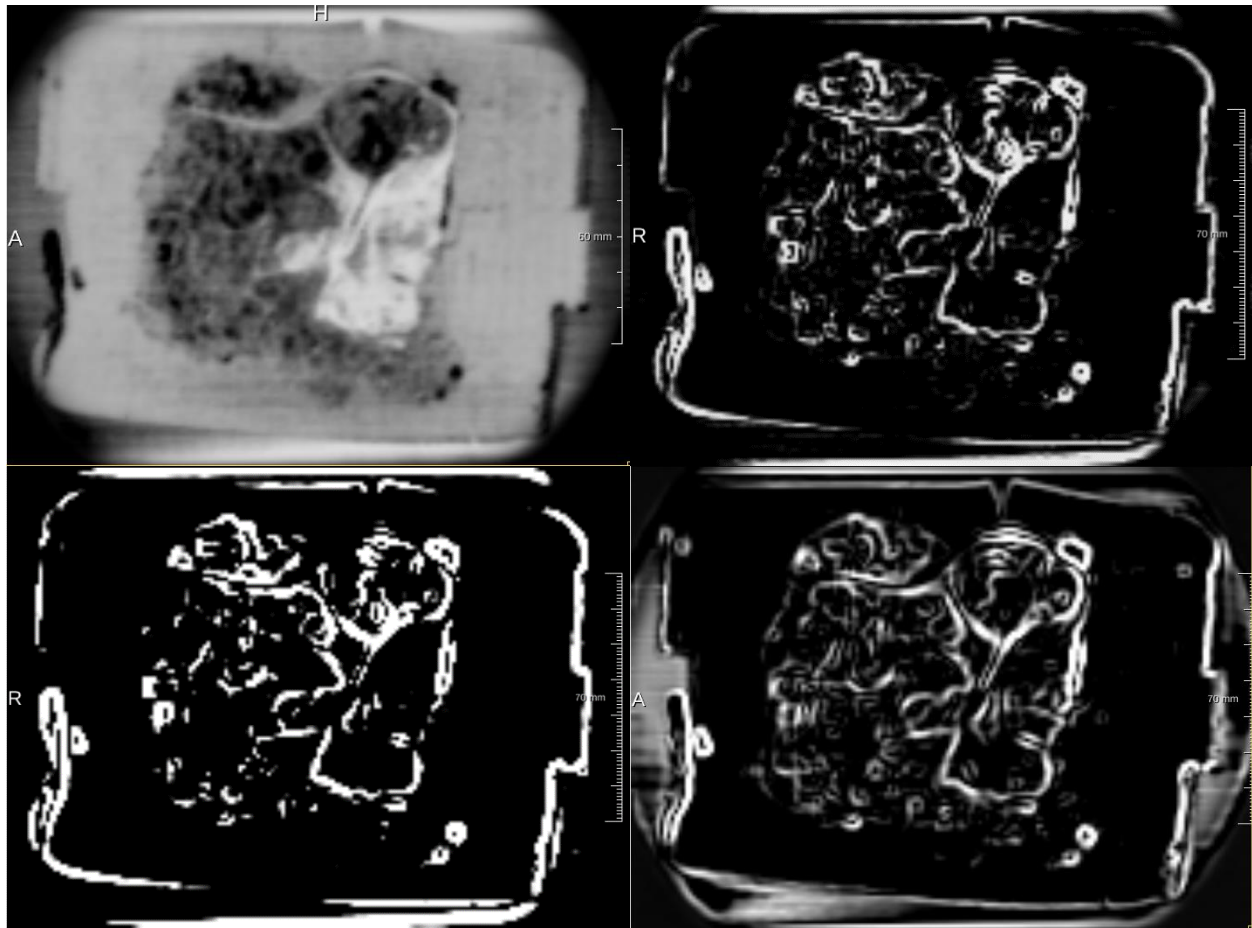
Figure 4.18: The results of applying Roberts cross and Sobel operators on another dataset. The top left image is the windowed input image, top right is Roberts cross, bottom left is 2D Sobel operator, and bottom right is 3D Sobel operator.

It can be seen from the above experimental results that derivative edge detectors are very susceptible to noise and fine structures in the images. This high sensitivity hinders us from separating out the principle region boundaries corresponding to the major tissue and cancer regions. To reduce the effect of these small intensity fluctuations inside the tissue areas, we first apply Gaussian smoothing to the input image prior to edge detection. The improved results are shown in Figure 4.19 and 4.20. Figure 4.19 shows the images obtained from the first dataset with Roberts cross operator by first smoothing the input image with Gaussian filter. We tested how the amount of smoothing affect the resulting images. The amount of smoothing is controlled by a

single parameter σ. Higher σ will give more smoothing. The images in Figure 4.19 are generated with sigma equal to 1.0, 1.5, and 2.0. As expected, the Gaussian smoothing has eliminated some smaller image structures, and emphasized the larger structures in the image.

Figure 4.20 shows the images obtained from the second dataset with Sobel 3D operator when applied to Gaussian smoothed input images with sigma equal to 1.0, 1.5, and 2.0. In this case, Gaussian smoothing has had a more profound effect on the edges. Output images are no longer mostly black and white, they now have large areas of grey. This may be because we are looking at cross-sections of 3D edges that are nearly parallel to the image plane.
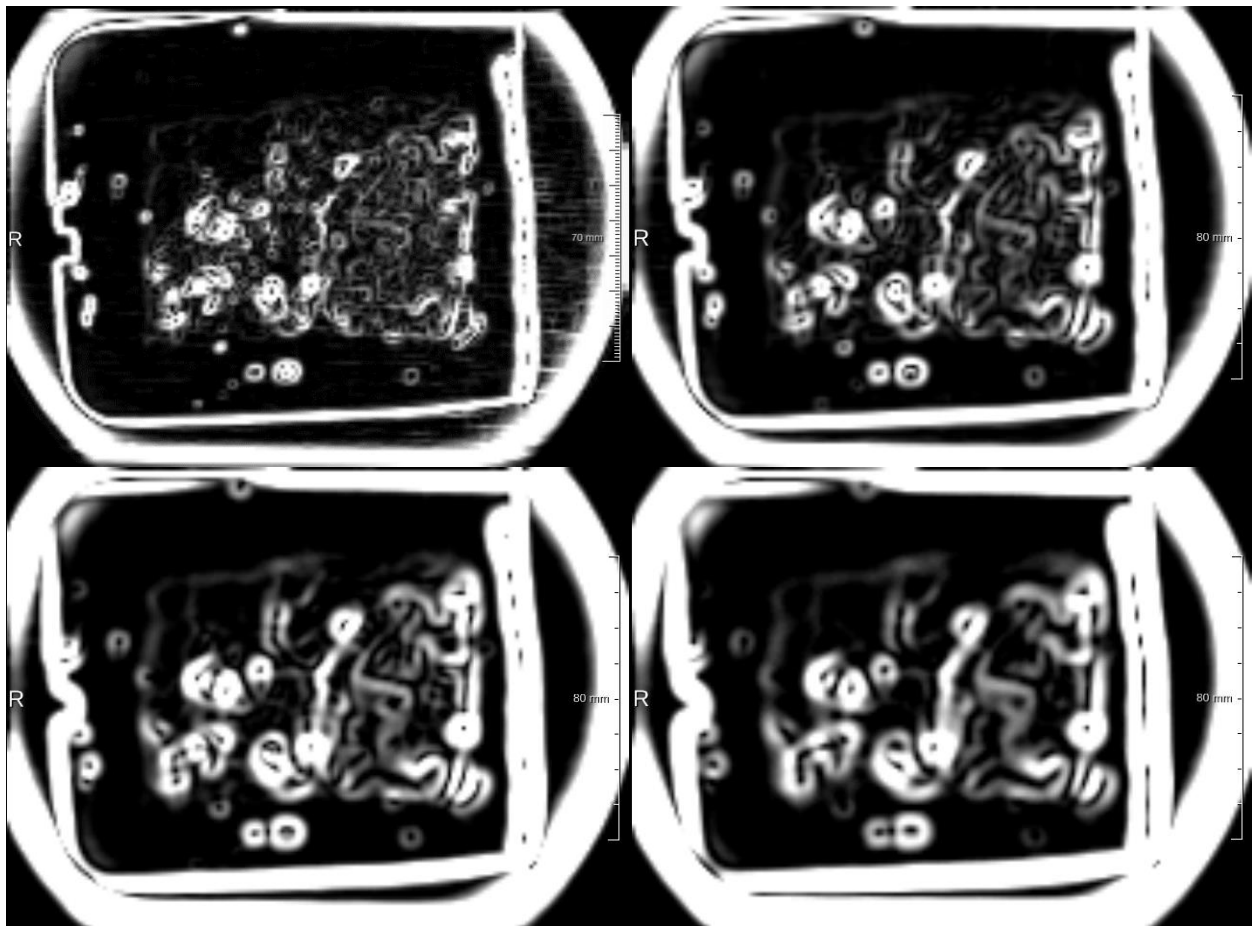

Figure 4.19: The effect of Roberts cross operator on unsmoothed input image (top left) vs. Gaussian smoothed input images with sigma equal to 1.0 (top right), 1.5 (bottom left), and 2.0 (bottom right).
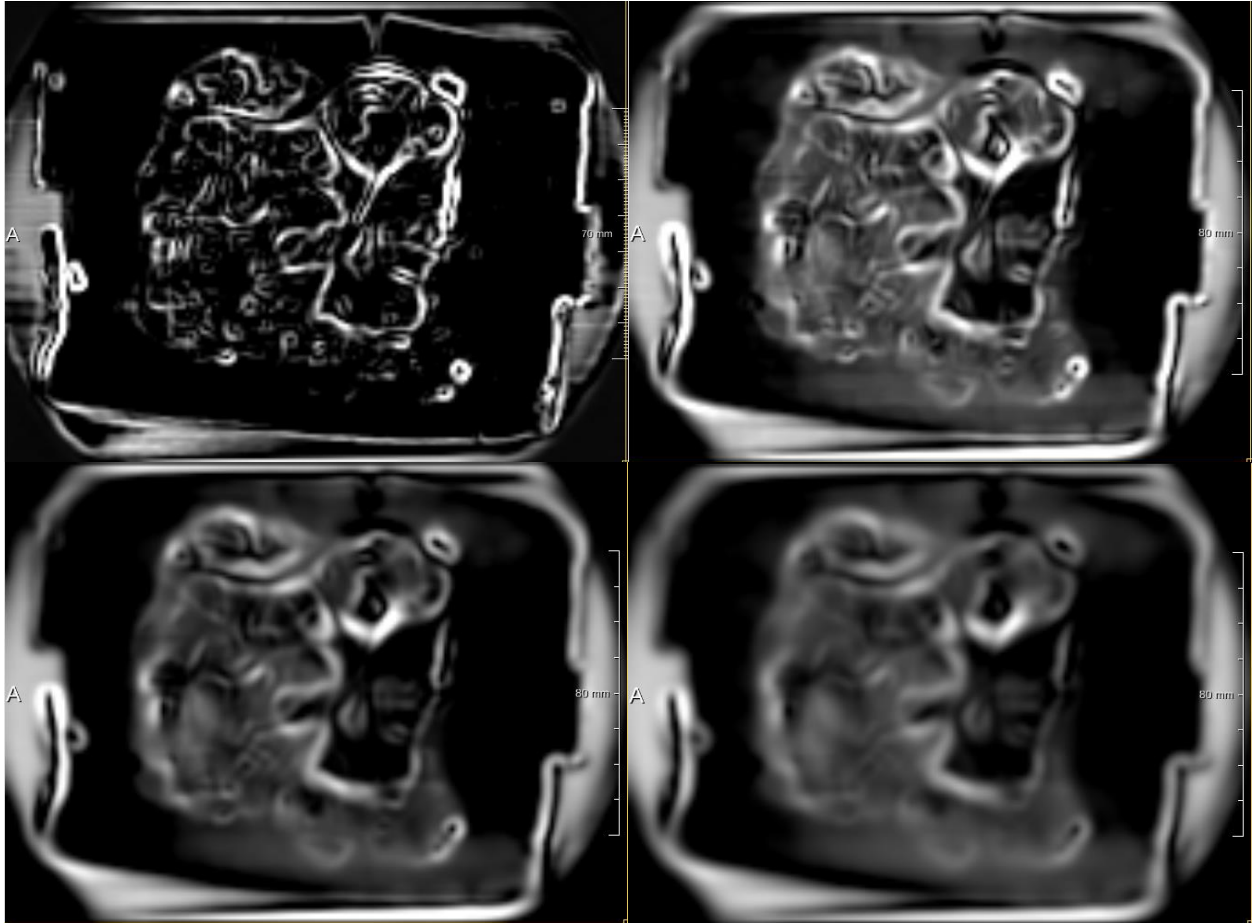
44

Figure 4.20: The effect of Sobel 3D operator on unsmoothed input image (top left) vs. Gaussian smoothed input images with sigma equal to 1.0 (top right), 1.5 (bottom left), and 2.0 (bottom right).

We also tested how effective the 2D Canny edge detector is on our THz data. In Figure 4.21, we experimented with three choices for the thresholding input parameter. In Canny's algorithm, both a low threshold and a high threshold need to be specified [27]. He also suggested that the ratio of the high to low threshold should be about three to one. The three images, from left to right in Figure 4.21, are generated with low threshold equal to 0.02, 0.03, and 0.04, and high threshold equal to 0.06, 0.09, and 0.12, respectively. Sigma values for the Gaussian filter in all three directions were kept constant at 2 in these images. Higher threshold results in fewer detected edges in the output image, as expected.

Next, we varied the sigma input parameters in all three dimensions while keeping the thresholds constant at 0.03 for low and 0.09 for high. The results are shown in Figure 4.22, from left to right, with sigma equal to 3, 4, and 5 in all three directions. Higher sigma value produces more blurring in the input image and reduces the effect of small intensity fluctuations in the fibroglandular regions, resulting in less number of detected edges in the output image.

Figure 4.23 shows the results of the Canny edge detector applied to another dataset. Since the edges in the raw data of this THz scan is much less pronounced than in the previous dataset, unsharp masking is first used to emphasize the edges in this image prior to using the Canny edge detector. We experimented with three input parameter combinations. The middle image generated with sigma equal to 5, low threshold equal to 0.03, and high threshold equal to 0.09 seems to give the best result.

Ideally, edges detected should form enclosing regions by edge linking. However, there is currently no implemented edge-linking module in *MeVisLab* so that edges in these images do not connect to form enclosed image regions. Overall, the Canny edge detector can be effective at detecting tissue and tumor boundaries when appropriate input parameters are found after several trials.

Figure 4.21: Results of the Canny edge detector on one of our dataset using low threshold value 0.02, 0.03, and 0.04, and high threshold value 0.06, 0.09, and 0.12, respectively.

Figure 4.22: Results of the Canny edge detector on the same dataset using sigma value equal to 3, 4, and 5, respectively.

Figure 4.23: Results of the Canny edge detector on another dataset preprocessed by unsharp masking. Sigma value used are 3, 5, and 7, with low threshold of 0.02, 0.03, and 0.04.

Region Growing

We evaluated how each of the three discussed region growing methods perform for two of our datasets. The first method, which expands regions simply by thresholding pixel value differences, can be carried out in *MeVisLab* using a built-in module. Figure 4.24 demonstrates its application to one of our datasets. This module allows the user to interactively select multiple initial seed points (in this case six) as well as the threshold interval size. The red shade in Figure 4.24 gives a reasonably well estimate of the cancer region. The main drawback of using this approach is that by only considering one cross section in the time domain, the performance of the segmentation depends critically on the choice of $t = t_0$ for the segmented cross section. As seen in the analysis of Figure 3.8, the differences between pixels from different regions vary among different time cross sections. There are time cross sections (such as at $t = 73 \ or \ 91$ in Figure

47

3.8) in which little difference is seen between pixels from tissue and tumor region. Thus, the effectiveness of this approach requires picking the right time cross section to segment with for each THz scan.

Our C++ program performs region growing by thresholding *L2* norm of the difference vector between two spatially adjacent time-sequence data or between the sequences at the candidate pixel location and the initial seed point location. Currently, our program takes in a single coordinate in the *x-y* plane as the seed point and expands its enclosing region based on the threshold set, which can be interactively changed using a keyboard. The results on the same dataset is shown in Figure 4.25. All the results shown for this dataset, however, failed to identify the full IDC region.

Figure 4.26 and 4.27 demonstrate region growing on another dataset. Our experiments show that the second approach (comparing only with the initial seed point) works considerably better in this dataset since the shape of the segmented cancer region matches more closely with the shape of the cancer region in the original image. It is also less sensitive to threshold adjustment compared to the first approach. Since only the seed point is being compared to, the success of this approach depends on picking the adequate seed point that represents the "average" characteristics of all the time sequences inside the region to be segmented. To mitigate this shortcoming, multiple initial seed points need to be specified to have a better chance of successful segmentation, which will be implemented in the future version of our program.
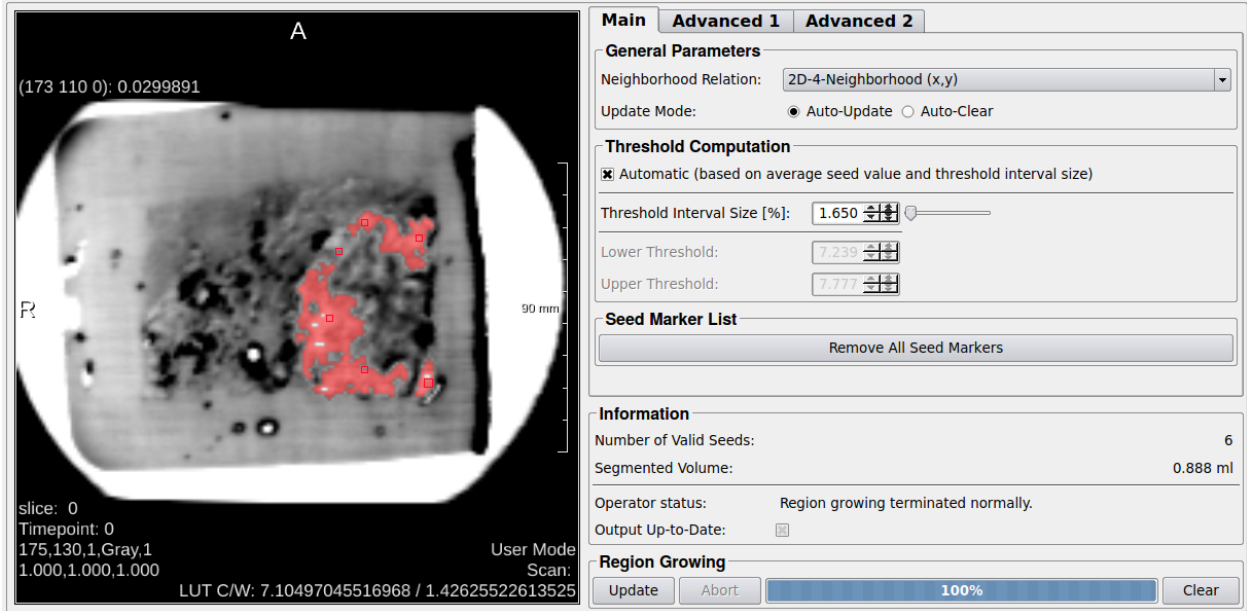
Figure 4.24: Region growing using the module implemented in *MeVisLab* to segment a time cross section for one of our datasets.
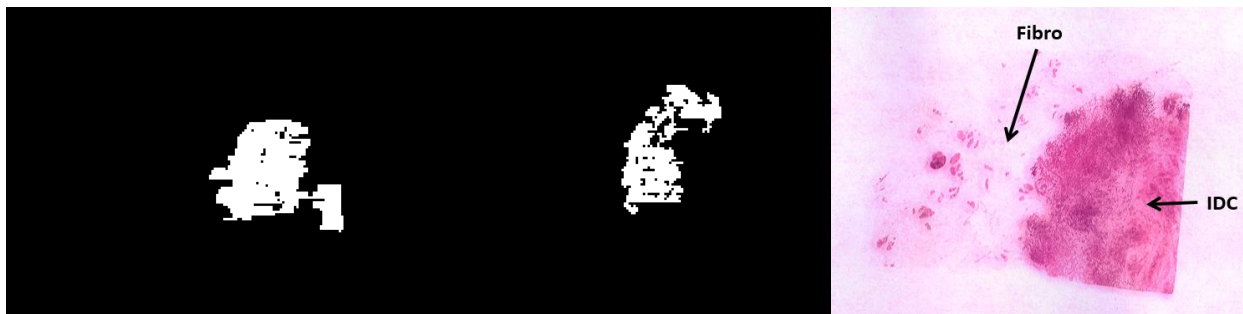

Figure 4.25: Region growing using our C++ program from a single seed point. The left image is generated by comparing adjacent time sequences. The middle image is generated by comparing with the initial seed point only. The right image is the histopathology image for comparison.
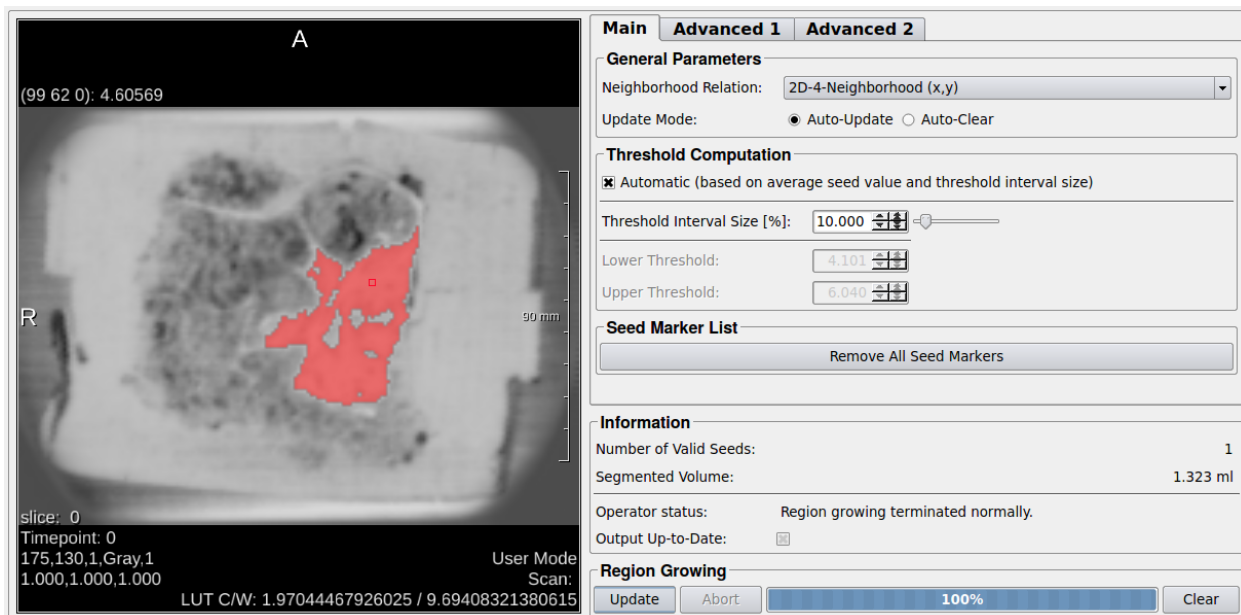
Figure 4.26: Region growing using the module implemented in *MeVisLab* to segment a time cross section for another dataset.
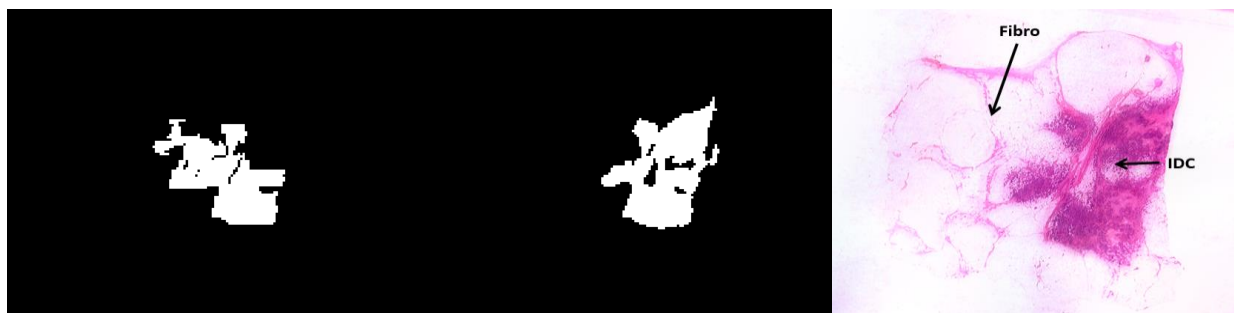

Figure 4.27: Region growing using our C++ program from a single seed point. The left image is generated by comparing adjacent time sequences. The middle image is generated by comparing with the initial seed point only. The right image is the histopathology image for comparison.

C.   Block Scan Enhancement and Visualization

We apply similar techniques to visualize the block scans, and the results on two of our datasets are shown here. Figure 4.29 shows time-domain cross section views of the tissue block from which the previously shown slice that contains a "C"-shape tumor region was cut. This block was imaged with a paraffin covering, and we can see that strong THz reflection was detected at that time-domain cross section which corresponds to the top surface of the imaged

block (top left image). Since the imaged tissue blocks are usually several hundred micrometers thick, time delay corresponds to distance in depth. That is, a time-domain cross section taken at a later time position usually reveals structural detail of the tissue block at a greater depth. Hence, the inside of the tissue block at different depths can be examined by taking time-domain cross sections at varying positions. Figure 4.29 shows three other cross sections taken at increasing depths below the tissue block surface. It is noticed that measurement values get weaker with increasing time delay, so intensity windowing needs to be adjusted to visualize each cross section properly. More noise is also noticed at deeper cross sections, which results in decreased signal-to-noise ratio (SNR) and introduces undesirable artifact. The cross section taken at a shallow depth right beneath the tissue surface, however, correlates fairly well with the slice scan shown previously. The "C"-shape tumor region shows a strong THz reflection response and is easily recognizable. The structural details inside the tissue block at deeper depth are harder to decipher at this point since we do not have possession of slice scans that correspond to these time-domain cross sections, nor do we have any histopathology references for them.

Figure 4.30 shows another demonstration of block scan visualization for the other dataset we experimented with previously. Cross sections of increasing depth are shown, and the first three images at relatively shallow depth correlates well with the tumor shape shown in the slice scans such as in Figure 4.4. The bottom right image is taken at a much deeper depth, and it bears few distinguishable details in it. Figure 4.31 shows a time-domain side view of the data. The tumor region beneath the paraffin covering and tissue surface can easily been seen after intensity windowing. However, more sample scans and histopathology references are needed to validate our observations.
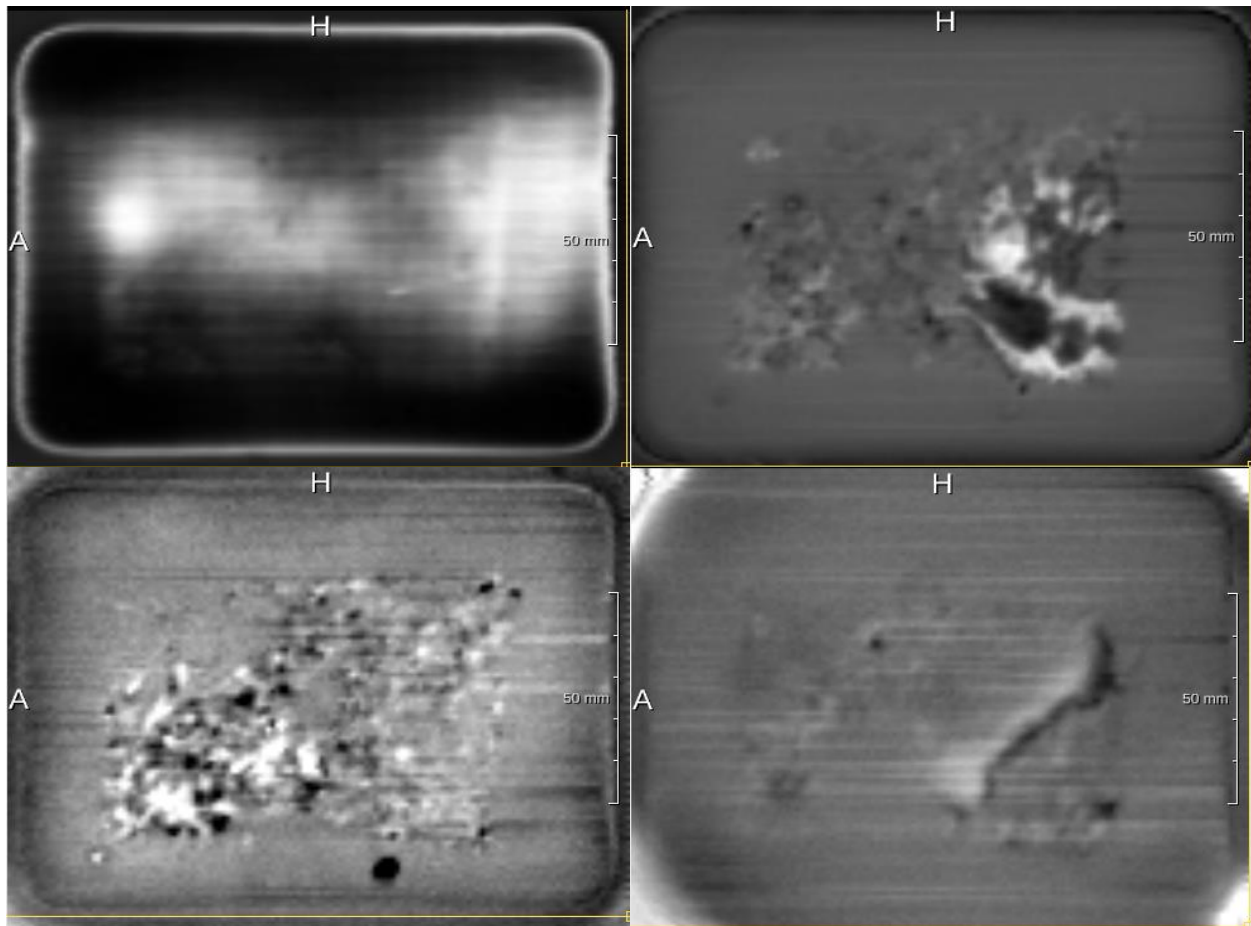
Figure 4.29: Time-domain cross sections at different time positions that correspond to increasing depths inside the imaged tissue block.
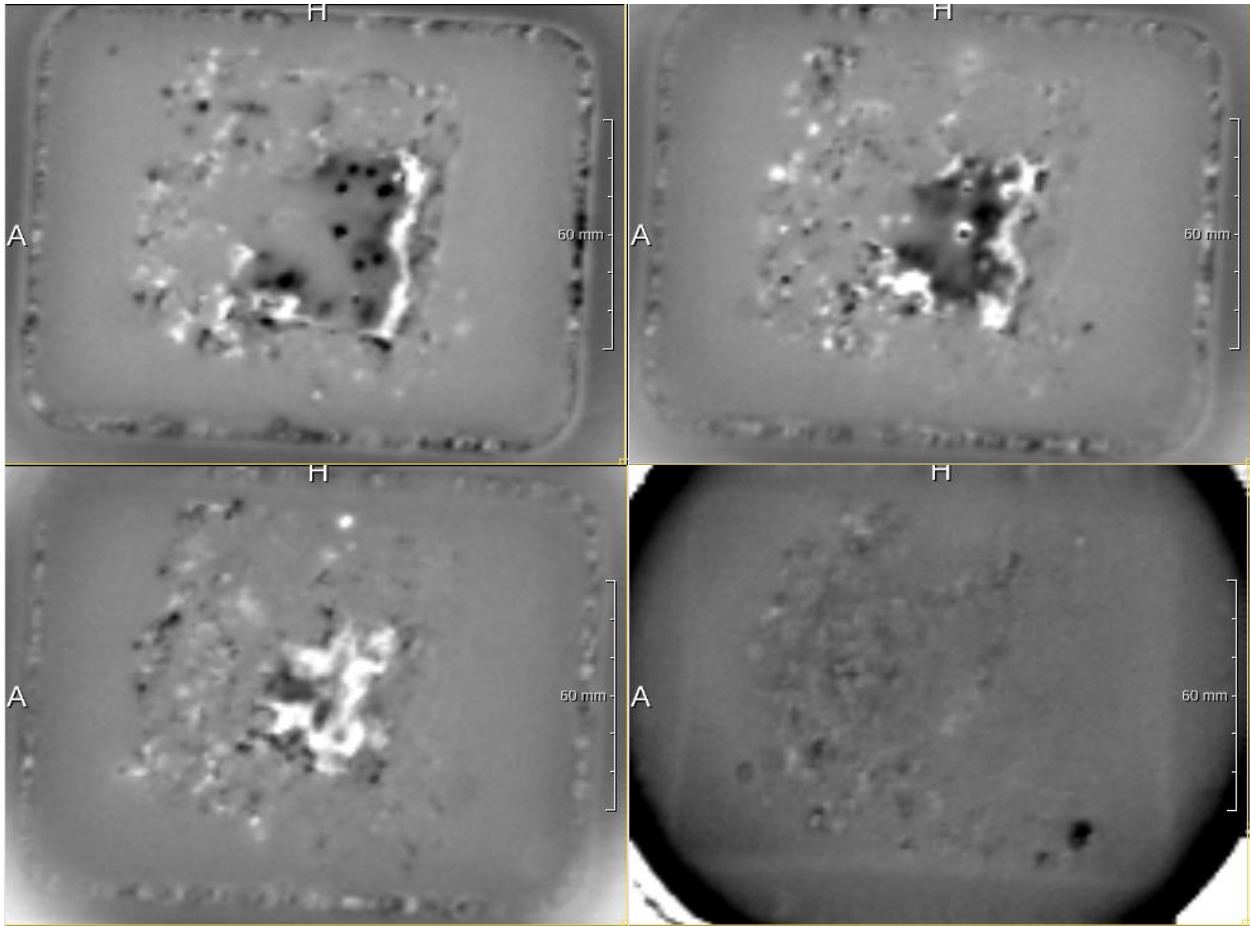
Figure 4.30: Time-domain cross sections at different time positions that correspond to increasing depths inside the imaged tissue block.

Figure 4.31: Time-domain side view of the same dataset. Tumor region beneath the paraffin covering and block surface shows a strong reflection response and is easily identifiable.

D.   Volume Visualization

MeVisLab provides a volume rendering module that can visualize three dimensional data interactively. Figure 4.32 shows an example of volume rendering on one of our slice scans. The rendered object is shown on the left of the displayed window. On the right, a variety of

illumination settings can be adjusted to produce different views of the rendered object. Figure

4.33 and 4.34 show three other such examples, one for a slice scan and two for block scans,

respectively.

The *MeVisLab* graphical user interface allows the user to interactively rotate the view

point to generate volume rendered images from different angles. This allows the user to better

understand the 3D shape and position of structures within the image relative to the bounding

volume. Unfortunately, this 3D visualization effect is difficult to illustrate in 2D static images in
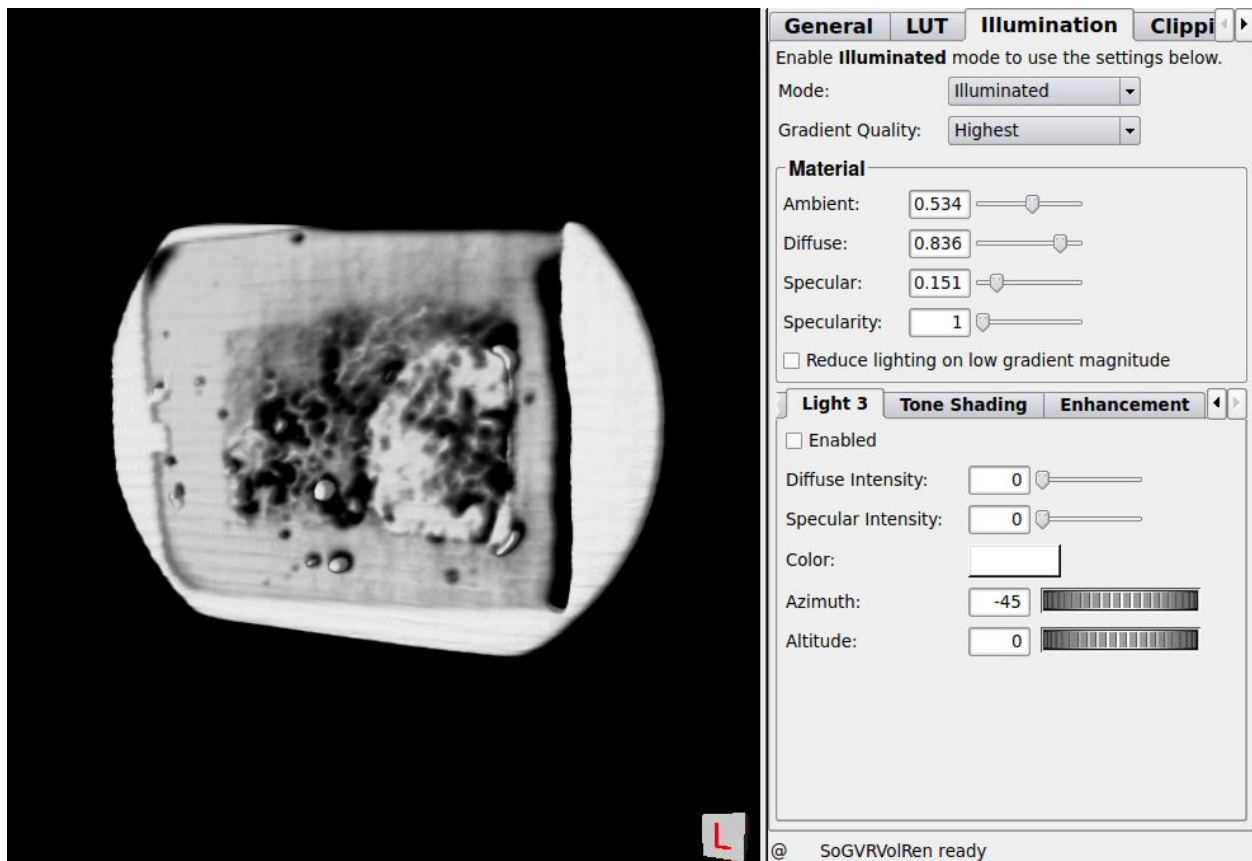
Figures 4.32, 4.33 and 4.34 below.

Figure 4.32: Volume rendering of a slice scan produced by *MeVisLab*.
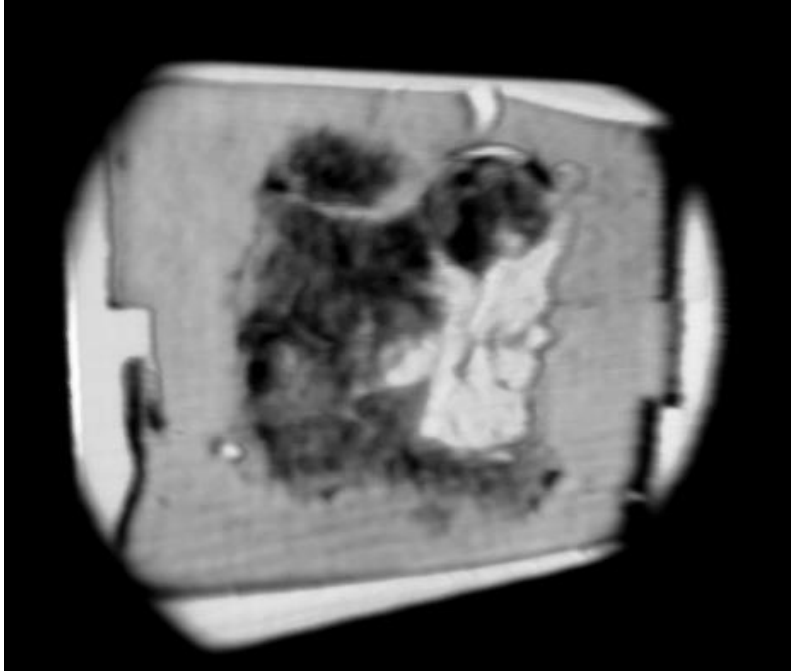
Figure 4.33: Volume rendering of a slice scan produced by *MeVisLab*.
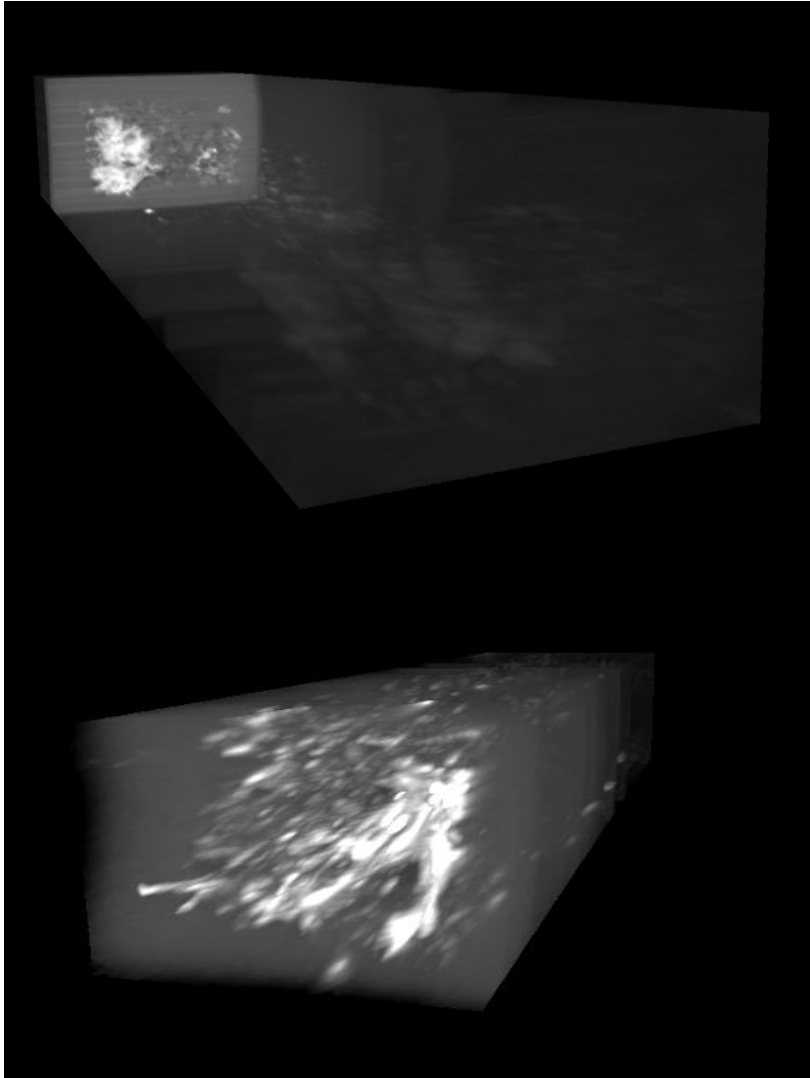
Figure 4.34: Volume rendering of two block scans produced by *MeVisLab*.

The rendered 3D views for the slice scans look very similar to the 2D time-domain cross section views shown previously. For the block scans, however, the 3D views are useful in that they provide a method to view the block as a whole and potentially gain some insight into the 3D structure of the tissue block which could not have been seen in the 2D cross section views. The top image in Figure 4.34 provides a clear view of the tumor region at the shallow depths inside the tissue block. The bottom image, although less distinctly outlined, still shows the approximate regions when the tumor resides inside the block. One issue that needs to be resolved is the

decreasing signal strengths when imaging depth increases. This issue is demonstrated by the faint

details in the left image of Figure 4.34. We tried several scaling methods to try to increase the

visibility of those details. More work still needs to be done to generate better 3D visualizations

of the deep sections of tissue blocks.

V.   Conclusion

A.   Contribution

In this thesis, a number of image enhancement and visualization techniques are explored to help us analyze pulsed THz images of breast cancer tissues. A summary of the pros and cons of these techniques is summarized below.

Method	Pros	Cons
Cross-Section Visualization	Straightforward method; rich details at the peak response	Visualization depends on chosen time cross-section
Scanline Registration	Fixed row misalignment; easy implementation	Extra computation time
Intensity Windowing	Specificity; customizable according to ROI	Manual adjustment required; setting changes with varying time cross-section
Histogram Equalization	Does not require user input specification	Less contrast enhancement than intensity windowing
Unsharp Masking	Edges appear sharpened; more detailed cross-section views	User input specification required
Laplacian Sharpening	Edges appear sharpened; more detailed cross-section views	User input specification required
Statistical Differencing	Time domain differencing generates unique cross-section views	Noise, distortion, and low contrast
Edge Detection (Roberts)	Acceptable results for 2D edge detection	Sensitive to intensity fluctuation
Edge Detection (2D Sobel)	Similar to Roberts detector	Sensitive to intensity fluctuation
Edge Detection (3D Sobel)	Slightly smoother edges detected, less sensitive to noise	Extra computation than 2D version
Edge Detection (Canny)	Accurate and clear edges detected that correspond to region boundaries well	User input specification required; trials and errors needed to get a clear result
Region Growing (2D)	Isolate tumor region well; interactive visualization	Result depends on seed selection and region edge strengths
Volume Visualization	Interactive 3D visualization	Manual adjustment required

Our results show that, by applying those enhancement and visualization methods to our THz image data, we can see rich details that were hidden in the unprocessed scans of tissue samples and extract information that are potentially invaluable to breast cancer diagnosis. Specifically, tumor regions and positive margins can be more easily identified after enhancing and segmentation, which demonstrates the potential of adopting THz imaging system during BCS in real-world clinical settings to facilitate surgeons in detecting the presence of positive margins. We evaluated the performance of each technique we experimented with, which could be helpful in the design and implementation of specialized THz image processing software that could be incorporated into THz imaging system in the future.

B.   Future Work

The processing techniques we considered so far are mostly based on spatial filtering. Frequency domain techniques have yet to be tried in future work to provide more comprehensive enhancements. More advanced histogram equalization algorithms, such as contrast limited adaptive histogram equalization (CLAHE), can be utilized to provide better contrast enhancement. Accurate noise models are not yet built, which are required for adequate de-noising. There exist other edge detection and segmentation algorithms that can be experimented with as well. 3D visualization of block scans has lots of room for improvement by utilizing other volume rendering techniques and data manipulation. Finally, more datasets are required for the application of advanced classification algorithms, the formation of rigorous validation of these approaches, and the quantification of the accuracy of these tumor detection techniques.

VI.   References

[1]   American Cancer Society. (2014). *Breast Cancer* [Online]. Available: http://www.cancer.org/acs/groups/cid/documents/webcontent/003090-pdf.pdf, last revised Aug. 19, 2015.

[2]   R. G. Pleijhuis *et al.*, "Obtaining Adequate Surgical Margins in Breast-Conserving Therapy for Patients with Early-Stage Breast Cancer: Current Modalities and Future Directions," *Ann. Surg. Oncol.*, vol. 16, pp. 2717–2730, Jul. 2009.

[3]   T. C. Bowman *et al.*, "Terahertz Imaging of Excised Breast Tumor Tissue on Paraffin Sections," *IEEE Trans. Antennas Propag.*, vol. 63, no. 5, pp. 2088–2097, May. 2015.

[4]   T. C. Bowman, "Experimental Terahertz Imaging and Spectroscopy of Ex-vivo Breast Cancer Tissue," M.S. thesis, Dept. Elect. Eng., Univ. Arkansas, 2014.

[5]   P. C. Ashworth *et al.*, "Terahertz Pulsed Spectroscopy of Freshly Excised Human Breast Cancer," *Opt. EXP.*, vol. 17, no. 15, pp. 12444–12454, Jul. 2009.

[6]   A. J. Fitzgerald *et al.*, "Terahertz Pulsed Imaging of Human Breast Tumors," *Radiology*, vol. 239, no. 2, pp. 533–540, May. 2006.

[7]   Y. Sun *et al.*, "A Promising Diagnostic Method: Terahertz Pulsed Imaging and Spectroscopy," *World J. Radiol.*, vol. 3, no. 3, pp. 55–65, Mar. 2011.

[8]   Teraphysics. (2015). *Understanding THz* [Online]. Available: http://www.teraphysics.com/understanding-thz.php

[9]   W. L. Chan *et al.*, "Imaging with Terahertz Radiation," *Rep. Prog. Phys.*, vol. 70, no. 8, pp. 1325–1379, Jul. 2007.

[10]   B. B. Hu and M. C. Nuss, "Imaging with Terahertz Waves," *Opt. Lett.*, vol. 20, no. 16, pp. 1716–1718, Aug. 1995.

[11]   D. Arnone *et al.*, "Terahertz Imaging Comes into View," *Phys. World*, vol. 13, no. 4, pp. 35–40, Apr. 2000.

[12]   C. Jansen *et al.*, "Terahertz Imaging: Applications and Perspectives," *Applied Optics*, vol. 49, no. 19, pp. E48–E57, Jul. 2010.

[13]   Y. Zhu *et al.*, "A Review of Optical NDT Technologies," *Sensors (Basel)*, vol. 11, no. 8, pp. 7773–7798, Aug. 2011.

[14]   X. Shen *et al.*, "Detection and Segmentation of Concealed Objects in Terahertz Images," *IEEE Trans. Image Process.*, vol. 17, no. 12, pp. 2465–2475, Dec. 2008.

[15]   R. M. Woodward *et al.*, "Terahertz Pulsed Imaging in Reflection Geometry of Human Skin Cancer and Skin Tissue," *Phys. in Med. and Bio.*, vol. 47, no.21, p. 3853–3863, Oct. 2002.

[16]   G. Reese *et al.*, "Using Terahertz Pulsed Imaging (TPI) to Identify Colonic Pathology," *Infrared, Millimeter and Terahertz Waves, 2008. IRMMW-THz 2008. 33rd International Conference on*, Sept. 2008

[17]   F. Wahaia *et al.*, "Detection of Colon Cancer by Terahertz Techniques," *Journal of Mole. Struc.*, vol. 1006, no. 1-3, pp. 77–82, Dec. 2011.

[18]   D. A. Crawley *et al.*, "Terahertz Pulse Imaging: A Pilot Study of Potential Applications in Dentistry," *Caries Research*, vol. 37, no. 5, pp. 352–359, Sep. 2003.

[19]   S. J. Oh *et al.*, "Study of Freshly Excised Brain Tissues Using Terahertz Imaging," *Biomedical Optics Expr.*, vol. 5, no. 8, pp. 2837–2842, Jul. 2014.

[20]   H. Hoshina *et al.*, "Terahertz Pulsed Imaging of Frozen Biological Tissues," *Infrared, Millimeter, and Terahertz Waves, 2009. IRMMW-THz 2009. 34th International Conference on,* Sep. 2009

[21]   N. Karpowicz *et al.*, "Comparision between Pulsed Terahertz Time-Domain Imaging and Continuous Wave Terahertz Imaging," *Semicond. Sci. Technol.*, vol. 20, no. 7, pp. S293–S299, Jun. 2005.

[22]   L. J. Solin *et al.*, "Relationship of Breast Magnetic Resonance Imaging to Outcome after Breast-Conservation Treatment with Radiation for Women with Early-Stage Invasive Breast Carcinoma or Ductal Carcinoma in Situ," *Journal of Clinical Oncology*, vol. 26, no. 3, pp. 386–91, Jan. 2008.

[23]   *MeVisLab* official website. (2015). Available: http://www.mevislab.de/

[24]   R. C. Gonzalez and R. E. Woods, "Intensity Transformation and Spatial Filtering", in *Digital Image Processing*, 3rd ed. Upper Saddle River, NJ: Pearson Prentice Hall, 2008, pp. 120–144.

[25]   W. K. Pratt, "Image Enhancement", in *Digital Image Processing*, 4th ed. Hoboken, NJ: John Wiley & Sons, 2007, pp. 288–291.

[26]   R. C. Gonzalez and R. E. Woods, "Image Segmentation", in *Digital Image Processing*, 3rd ed. Upper Saddle River, NJ: Pearson Prentice Hall, 2008, pp. 689–794.

[27]   J. Canny, "A Computational Approach to Edge Detection", *IEEE Trans. Pattern Anal. Mach. Intell.*, vol. PAMI-8, no. 6, pp. 679–698, Nov. 1986.

[28]   *ITK* Examples (2015), *Detect Edges with Canny Edge Detection Filter* [online].
       Available: http://itk.org/ITKExamples/src/Filtering/ImageFeature/
       DetectEdgesWithCannyFilter/Documentation.html

[29]   *ITK* official website. (2015). Available: http://www.itk.org/

[30]   M. Levoy, "Display of Surfaces from Volume Data", IEEE CG&A, May 1988.

[31]   Wikipedia. (2015). *Volume Rendering* [online]. Avaible:
       https://en.wikipedia.org/wiki/Volume_rendering#/media/File:CTWristImage.png

[32]   B. St. Peter *et al.*, "Development and Testing of a Single Frequency Terahertz Imaging
       System for Breast Cancer Detection," *IEEE J. Biomed. Health Inform.*, vol. 17, no. 4, pp.
       785–797, Jul. 2013.